

MultiView Diffusion Maps

Ofir Lindenbaum¹ Arie Yeredor¹ Moshe Salhov² Amir Averbuch²

¹School of Electrical Engineering, Tel Aviv University, Israel

²School of Computer Science, Tel Aviv University, Israel

10-February-2016

Abstract

In this paper, a reduced dimensionality representation is learned from multiple views of the processed data. These multiple views can be obtained, for example, when the same underlying process is observed using several different modalities, or measured with different instrumentation. The goal is to effectively utilize the availability of such multiple views for various purposes such as non-linear embedding, manifold learning, spectral clustering, anomaly detection and non-linear system identification. The proposed method, which is called multiview, exploits the intrinsic relation within each view as well as the mutual relations between views. This is achieved by defining a cross-view model in which an implied a random walk process between objects is restrained to hop between the different views. This multiview method is robust to scaling and it is insensitive to small structural changes in the data. Within this framework, new diffusion distances are defined to analyze the spectra of the implied kernels. The applicability of the multiview approach is demonstrated on both artificial and real data.

I. INTRODUCTION

High dimension big data exist in various fields and it is difficult to analyze them as is. Extracted features are useful in analyzing these datasets. Some prior knowledge or modeling is required in order to identify the essential features. On the other hand, dimensionality reduction methods are purely unsupervised aiming to find a low dimensional representation that is based on the *intrinsic geometry* of the analyzed dataset that includes the connectivities among multidimensional data points within the dataset. A “good” dimensionality reduction methodology reduces the complexity of a data processing while preserving the coherency of the original data such that clustering, classification, manifold learning and many other data analysis tasks can be applied effectively in the reduced space. Many methods such as Principal Component Analysis (PCA) [1], Multidimensional Scaling (MDS) [2], Local Linear Embedding [3], Laplacian Eigenmaps [4], Diffusion Maps (DM) [5] and more have been proposed to achieve dimensionality reduction that preserve its data coherency. Exploiting the low dimensional representation yields various applications such as face recognition that is based on Laplacian Eigenmaps [4], Non-linear independent component analysis with DM [6], Musical Key extraction using DM [7], and many more. The DM framework extends and enhances ideas from other methods by utilizing a stochastic Markov matrix that is based on local affinities between multidimensional data points to identify a lower dimension representation for the data. All the mentioned methods do not consider the possibility of having more than one view to represent the same process. An additional view can provide meaningful insight regarding the dynamical process that has generated and governed the data.

In this paper, we consider learning from data that is analyzed by multiple views. The goal is to effectively utilize multiple views such as non-linear embedding, multi-view manifold learning, spectral clustering, anomaly detection and non-linear system identification to achieve better analysis of high dimension big data. Most dimensionality reduction methods suggest to concatenate the datasets into a single vector space. However, this methodology is sensitive to scalings of each data component. It does not utilize for example the fact that noise in both datasets could be uncorrelated. It assumes that both datasets lie in one high dimensional space which is not always true.

The problem of learning from two views has been studied in the field of spectral clustering. Most of these studies have been focused on classification and clustering that are based on spectral characteristics of the data while using two or more sampled views. Some approaches, which address this problem, are Bilinear Model [8], Partial Least Squares [9] and Canonical Correlation Analysis [10]. These methods are powerful for learning the relation between different views but do not provide separate insights or combined into the low dimensional geometry or structure of each view. Recently, a few kernel based methods (e.g [11]) propose a model of co-regularizing kernels in both views in a way that resembles joint diagonalization. It is done by searching for an orthogonal transformation that maximizes the diagonal terms of the kernel matrices obtained from all views. A penalty term, which incorporates the disagreement between clusters from the views, was added. Their algorithm is based on alternating maximization procedure. A mixture of Markov chains is proposed in [12] to model multiple views in order to apply spectral clustering. It deals with two cases in graph theory: directed and undirected graph where the second case is related to our work. This approach converges the undirected graph problem to a Markov chains averaging where each is constructed separately within the views. A way to incorporate a given multiple metrics for the same data using a cross diffusion process is described in [13]. However, the applicability of the suggested approach is limited only for a clustering

task. An iterative algorithm for spectral clustering is proposed in [14]. The idea is to iteratively modify each view using the representation of the other view. The problem of two manifolds, which were derived from the same data (i.e two views), is described in [15]. This approach is similar to Canonical Correlation Analysis [16] that seeks a linear transformation that maximizes the correlation among the views. It demonstrates the power of this method in canceling uncorrelated noise present in both views. Furthermore, [15] applies its method to a non-linear system identification task. A similar approach is proposed in [17]. It suggests data modeling that uses a bipartite graph and then, based on the ‘minimum-disagreement’ algorithm, partitions the dataset. This approach attempts to minimize the cluster’s disagreement between multiple views.

In this work, we present a framework based on the construction in [17] and show that this approach is a special case of a more general diffusion based process. We build and analyze a new framework that generalizes the random walk model while utilizing multiple views. Our proposed method utilizes the intrinsic relation within each view as well as the mutual relations between views. The multiview is achieved by defining a cross diffusion process in which a special structured random walk is imposed between the various views. The multiview method is robust to scalings of each view and it is insensitive to small structural changes in the data. Within this framework, new diffusion distances are defined to analyze the spectra of the new kernels and compute the infinitesimal generator to where the multiview-based our kernel converges. The advantages of the proposed method for manifold learning and spectral clustering are explored.

The paper has the following structure: Background is given in section II. Section III presents and analyzes the multiview framework. Section IV studies the asymptotics properties of the proposed kernel $\widehat{\mathbf{K}}$ (Eq. 5). Section V presents the experimental results.

II. BACKGROUND

A. General dimensionality reduction framework

Consider a high dimensional dataset $\mathbf{X} = \{\mathbf{x}_1, \mathbf{x}_2, \mathbf{x}_3, \dots, \mathbf{x}_M\} \in \mathbb{R}^{M \times N}$, $\mathbf{x}_i \in \mathbb{R}^N$, $i = 1, \dots, M$. The goal is to find a low dimensional representation $\mathbf{Z} = \{\mathbf{z}_1, \mathbf{z}_2, \mathbf{z}_3, \dots, \mathbf{z}_M\} \in \mathbb{R}^{M \times S}$, $\mathbf{z}_i \in \mathbb{R}^S$, $i = 1, \dots, M$, such that $S \ll N$ and the local connectivities among the multidimensional data points are preserved. This problem setup is based on the assumption that the data is represented (viewed) by a single vector space (single view).

B. Diffusion Maps (DM)

DM [5] is a dimensionality reduction method that finds the intrinsic geometry in the data. This framework is highly effective when the data is densely sampled from some low dimensional manifold that is not linear. Given a high dimensional dataset \mathbf{X} , the DM framework contains the following steps:

- 1) A kernel function $\mathcal{K} : \mathbf{X} \times \mathbf{X} \rightarrow \mathbb{R}$ is chosen. It is represented by a matrix $\mathbf{K} \in \mathbb{R}^{M \times M}$ which satisfies for all $(\mathbf{x}_i, \mathbf{x}_j) \in \mathbf{X}$ the following properties: Symmetry: $K_{i,j} = \mathcal{K}(\mathbf{x}_i, \mathbf{x}_j) = \mathcal{K}(\mathbf{x}_j, \mathbf{x}_i)$, positive semi-definiteness: $\mathbf{v}_i^T \mathbf{K} \mathbf{v}_i \geq 0$ for all $\mathbf{v}_i \in \mathbb{R}^M$ and $\mathcal{K}(\mathbf{x}_i, \mathbf{x}_j) \geq 0$. These properties guarantee that the matrix \mathbf{K} has real eigenvectors and non-negative real eigenvalues. Gaussian kernel is a common example where $K_{i,j} = \exp\{-\frac{\|\mathbf{x}_i - \mathbf{x}_j\|^2}{2\sigma_x^2}\}$ with an L_2 norm as the affinity measure between two data vectors;
- 2) By normalizing the kernel using \mathbf{D} where $D_{i,i} = \sum_j K_{i,j}$, we compute the following matrix elements:

$$P_{i,j}^x = \mathcal{P}(\mathbf{x}_i, \mathbf{x}_j) = [\mathbf{D}^{-1} \mathbf{K}]_{i,j}. \quad (1)$$

The resulting matrix $\mathbf{P}^x \in \mathbb{R}^{M \times M}$ can be viewed as the transition kernel of a (fictitious) Markov chain on \mathbf{X} such that the expression $[(\mathbf{P}^x)^t]_{i,j} = p_t(\mathbf{x}_i, \mathbf{x}_j)$ describes the transition probability from point \mathbf{x}_i to point \mathbf{x}_j in t steps.

- 3) Spectral decomposition is applied to matrix \mathbf{P}^x or to one of its powers $(\mathbf{P}^x)^t$ to obtain a sequence of eigenvalues $\{\lambda_m\}$ and normalized eigenvectors $\{\psi_m\}$ that satisfies $\mathbf{P}^x \psi_m = \lambda_m \psi_m$, $m = 0, \dots, M-1$;
- 4) Define a new representation for the dataset \mathbf{X}

$$\Psi_t(\mathbf{x}_i) : \mathbf{x}_i \mapsto [\lambda_1^t \psi_1(i), \lambda_2^t \psi_2(i), \lambda_3^t \psi_3(i), \dots, \lambda_{M-1}^t \psi_{M-1}(i)]^T \in \mathbb{R}^{M-1}, \quad (2)$$

where t is the selected number of steps and $\psi_m(i)$ denotes the i^{th} element of ψ_m .

The main idea behind this representation is that the Euclidian distance between two data points in the new representation is equal to the weighted L_2 distance between the conditional probabilities $p_t(\mathbf{x}_i, \cdot)$, and $p_t(\mathbf{x}_j, \cdot)$, $i, j = 1, \dots, M$ (the i -th and j -th rows of \mathbf{P}^t). The following is referred as the Diffusion Distance

$$\mathcal{D}_t^2(\mathbf{x}_i, \mathbf{x}_j) = \|\Psi_t(\mathbf{x}_i) - \Psi_t(\mathbf{x}_j)\|^2 = \sum_{m \geq 1} \lambda_m^{2t} (\psi_m(i) - \psi_m(j))^2 = \|p_t(\mathbf{x}_i, \cdot) - p_t(\mathbf{x}_j, \cdot)\|_{\mathbf{W}^{-1}}^2, \quad (3)$$

where \mathbf{W} is a diagonal matrix with elements $W_{i,i} = \phi_0(i) = \frac{D_{i,i}}{\sum_{i=1}^M D_{i,i}}$. This equality is proven in [5].

5) The desired accuracy $\delta \geq 0$ is chosen for the diffusion distance defined by Eq. 3 such that $s(\delta, t) = \max\{\ell \in \mathbb{N} \text{ such that } |\lambda_\ell|^t > \delta |\lambda_1|^t\}$. By using δ , a new mapping of $s(\delta, t)$ dimensions is defined as

$$\Psi_t^{(\delta)} : \mathbf{X} \rightarrow [\lambda_1^t \psi_1(i), \lambda_2^t \psi_2(i), \lambda_3^t \psi_3(i), \dots, \lambda_s^t \psi_s(i)]^T \in \mathbb{R}^{s(\delta, t)}.$$

This approach has been found useful in various fields. As previously noted, it is limited to a single view representation. A common extension of this approach to multiple views is to do data concatenation from all views into a single vector space and then apply to it the diffusion framework. This approach assumes orthogonality of the sampled dimension which is an unrealistic assumption in many cases. Furthermore, this approach can create redundancy in some dimensions and requires scaling of each dimension separately such that none is preferable over the others. Previous studies such as [18], [19] apply the DM framework to each view separately and then incorporated the learned mapping from various views. However they do not exploit the mutual relations which might exist between the various views in order to create and utilize the correct mapping.

III. MULTIVIEW DIMENSIONALITY REDUCTION

Problem Formulation: Given two sets of observations $\mathbf{X} = \{\mathbf{x}_1, \mathbf{x}_2, \mathbf{x}_3, \dots, \mathbf{x}_M\} \in \mathbb{R}^{D_1}$ and $\mathbf{Y} = \{\mathbf{y}_1, \mathbf{y}_2, \mathbf{y}_3, \dots, \mathbf{y}_M\} \in \mathbb{R}^{D_2}$, which are views with bijective correspondence that were sampled from the same physical phenomena. The goal is to find a lower dimensional representation for each view that preserves the interactions between multidimensional data points and between the views \mathbf{X} and \mathbf{Y} .

A. Multiview Diffusion Maps

We begin by generalizing the DM framework for handling a multiview scenario. Our goal is to impose a random walk model using the local connectivities between data points within both views. Our way to incorporate the connectivities is by restraining the random walker to “hop” between views in each step. The first step in this construction is to choose a symmetric and positive-semi-definite kernel functions one for each view such that $\mathcal{K}^x : \mathbf{X} \times \mathbf{X} \rightarrow R$ and $\mathcal{K}^y : \mathbf{Y} \times \mathbf{Y} \rightarrow R$, as explained in Section II-B. A common choice is a Gaussian kernel. These kernels should capture the local intrinsic geometry of each view and ignore the global geometry. We form from \mathcal{K}^x and \mathcal{K}^y , a large row-stochastic matrix of size $2M \times 2M$ as follows: first we compute the matrix product $\mathbf{K}^z = \mathbf{K}^x \mathbf{K}^y$ between the kernels \mathcal{K}^x and \mathcal{K}^y such that (for a kernel)

$$K_{i,j}^z = \sum_m K_{i,m}^x K_{m,j}^y = \sum_m e^{-\frac{\|\mathbf{x}_i - \mathbf{x}_m\|^2}{2\sigma_x^2}} e^{-\frac{\|\mathbf{y}_m - \mathbf{y}_j\|^2}{2\sigma_y^2}} = [\mathbf{K}^z]_{i,j}, \quad (4)$$

then, the generalized multiview kernel is formed by the following matrix

$$\widehat{\mathbf{K}} = \begin{bmatrix} \mathbf{0}_{M \times M} & \mathbf{K}^z \\ (\mathbf{K}^z)^T & \mathbf{0}_{M \times M} \end{bmatrix}. \quad (5)$$

Finally, by using the diagonal matrix $\widehat{\mathbf{D}}$ where $\widehat{D}_{i,i} = \sum_j \widehat{K}_{i,j}$, we compute the normalized row-stochastic matrix

$$\widehat{\mathbf{P}} = \widehat{\mathbf{D}}^{-1} \widehat{\mathbf{K}}, \quad \widehat{P}_{i,j} = \frac{\widehat{K}_{i,j}}{\widehat{D}_{i,i}}, \quad (6)$$

which describes the probability matrix of a Markov random walk between the data points of \mathbf{X} and \mathbf{Y} . The block anti-diagonal form of $\widehat{\mathbf{K}}$ is symmetric and the normalized version $\widehat{\mathbf{P}}$ provides a probabilistic interpretation to the construction (explained in III-C).

B. Alternative Multiview Approaches

In this section, we describe two additional methods for incorporating different views. We do not analyze these approaches but use them as references for comparisons in the experimental evaluations.

1. Kernel product (Hadamard product):

The kernel matrices \mathcal{K}^x and \mathcal{K}^y are multiplied element wise $\mathbf{K}^\circ = \mathbf{K}^x \circ \mathbf{K}^y$, $K_{i,j}^\circ = K_{i,j}^x \cdot K_{i,j}^y$ where \circ is the Hadamard matrix product. Then, normalization by the sum of rows results in a row stochastic matrix \mathbf{P}° becomes

$$P_{i,j}^\circ = [D^{\circ-1} \mathbf{K}^\circ]_{i,j}, \quad (7)$$

where $D_{i,i}^\circ = \sum_j K_{i,j}^\circ$. This approach can be described by the framework in [5].

Lema 1. In the special case of a Gaussian kernel with $\sigma_x = \sigma_y$ in Eq. (4), the resulting matrix \mathbf{K}° is equal to the matrix \mathbf{K}^w constructed using the concatenated vector $\mathbf{w}_i = [\mathbf{x}_i^T, \mathbf{y}_i^T]^T$ such that $K_{i,j}^w = \exp\{-\frac{\|\mathbf{w}_i - \mathbf{w}_j\|^2}{2\sigma_w^2}\}$.

In more general cases where σ° is set explicitly as the vector $\sigma^\circ = [\sigma_x, \sigma_y]$. We use

$$\sigma^\circ = \sqrt{\sigma_x^2 + \sigma_y^2}. \quad (8)$$

This approach, which corresponds to [5], will be referred as the Kernel Product DM in the following sections.

2. Additive kernel:

Kernels' sum is defined by $\mathbf{K}^+ = \mathbf{K}^x + \mathbf{K}^y$. This kernel is normalized by the sum of the rows. This random walk sums the step probabilities from each view. This approach is computationally inexpensive in comparison to the other methods, however, it is unclear what geometry it reveals. If noise exists in the sampled data, the new kernel \mathbf{K}^+ will contain the sum of noises from both views. This approach was proposed in [12]. We define the normalized row-stochastic version of \mathbf{K}^+ as

$$P_{i,j}^+ = [D^{+1} \mathbf{K}^+]_{i,j}, \quad (9)$$

where $D_{i,i}^+ = \sum_j K_{ij}^+$. This approach, which corresponds to [12], will be referred as Kernel Sum DM in the following sections.

C. Probabilistic interpretation of $\hat{\mathbf{P}}$

In our proposed construction (Eqs. (4), (5) and (6)), the entries $[\hat{\mathbf{P}}^t]_{i,j} = \hat{p}_t(\mathbf{x}_i, \mathbf{x}_j)$ denote for each $i, j = 1, \dots, M$, the transition probability from node \mathbf{x}_i to node \mathbf{x}_j in t time steps by ‘‘hopping’’ between the views \mathbf{X} and \mathbf{Y} in each time step. Note that due to the block-anti-diagonal structure of $\hat{\mathbf{K}}$ (and $\hat{\mathbf{P}}$ (Eq. (6))), this probability is zero for odd values of t . However, for even values of t , this probability is nonzero describing an even time transition from view \mathbf{X} through view \mathbf{Y} and back to \mathbf{X} . In the same way, $[\hat{\mathbf{P}}^t]_{i+M,j+M} = \hat{p}_t(\mathbf{y}_i, \mathbf{y}_j)$ denotes the transition probability from node \mathbf{y}_i to node \mathbf{y}_j ($i, j = 1, \dots, M$) in t time steps. Likewise, $[\hat{\mathbf{P}}^t]_{i,j+M} = \hat{p}_t(\mathbf{x}_i, \mathbf{y}_j)$ denotes the transition probability from node \mathbf{x}_i to node \mathbf{y}_j ($i, j = 1, \dots, M$) in t time steps. Note that this probability is nonzero only for odd values of t . This probability takes into consideration all the various possibilities of crossing from node \mathbf{x}_i to node \mathbf{y}_j by propagating in view \mathbf{X} and then in view \mathbf{Y} . Figure 1 illustrates the multiview transition probabilities compared to a single view approach using two Swiss-roll manifolds.

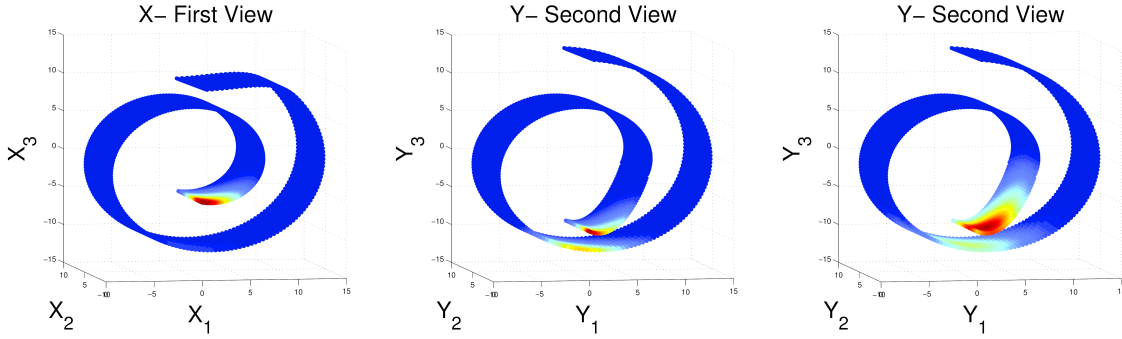


Fig. 1: Left: Swiss roll sampled from View-I (\mathbf{X}), colored by the single view probability of transition ($t = 1$) from \mathbf{x}_1 to \mathbf{x}_\cdot . Middle: second Swiss roll sampled from View-II (\mathbf{Y}), colored by the single view probability of transition ($t = 1$) from \mathbf{y}_1 to \mathbf{y}_\cdot . Right: the multiview probabilities of transition ($t = 1$) from \mathbf{x}_i to \mathbf{y}_\cdot .

D. Spectral decomposition

In this section, we show how to efficiently compute the spectral decomposition of $\hat{\mathbf{P}}$ (Eq. (6)). The matrix $\hat{\mathbf{P}}$ is algebraically similar to the symmetric matrix $\hat{\mathbf{P}}_s$ where $\hat{\mathbf{P}}_s = \hat{\mathbf{D}}^{1/2} \hat{\mathbf{P}} \hat{\mathbf{D}}^{-1/2} = \hat{\mathbf{D}}^{-1/2} \hat{\mathbf{K}} \hat{\mathbf{D}}^{-1/2}$. Therefore, both $\hat{\mathbf{P}}$ and $\hat{\mathbf{P}}_s$ share the same set of eigenvalues $\{\lambda_m\}$. Due to symmetry of the matrix $\hat{\mathbf{P}}_s$, it has a set of $2M$ real eigenvalues $\{\lambda_i\}_{i=0}^{2M-1} \in \mathbb{R}$ and a corresponding real orthogonal eigenvectors $\{\pi_m\}_{m=0}^{2M-1} \in \mathbb{R}^{2M}$, thus, $\hat{\mathbf{P}}_s = \mathbf{\Pi} \mathbf{\Lambda} \mathbf{\Pi}^T$. By denoting $\mathbf{\Psi} = \hat{\mathbf{D}}^{-1/2} \mathbf{\Pi}$ and $\mathbf{\Phi} = \hat{\mathbf{D}}^{1/2} \mathbf{\Pi}$, we conclude that the set $\{\psi_m, \phi_m\}_{m=0}^{2M-1} \in \mathbb{R}^{2M}$ denotes the right and the left eigenvectors of $\hat{\mathbf{P}} = \mathbf{\Psi} \mathbf{\Lambda} \mathbf{\Phi}^T$, respectively, satisfying $\psi_i^T \phi_j = \delta_{ij}$. In the sequel, we use the symmetric matrix $\hat{\mathbf{P}}_s$ to simplify the analysis.

To avoid the spectral decomposition of a $2M \times 2M$ matrix $\hat{\mathbf{P}}_s$, the spectral decomposition of $\hat{\mathbf{P}}_s$ can be computed using the Singular Value Decomposition (SVD) of the matrix $\bar{\mathbf{K}}^z = \mathbf{D}^{rows-1/2} \mathbf{K}^z \mathbf{D}^{cols-1/2}$ of size $M \times M$ where $D_{i,i}^{rows} = \sum_{j=1}^M K_{i,j}^z$ and $D_{j,j}^{cols} = \sum_{i=1}^M K_{i,j}^z$ are diagonal matrices. Theorem 1 enables us to form the eigenvectors of $\hat{\mathbf{P}}$ as a concatenation of the singular vectors of $\bar{\mathbf{K}}^z$ (Eq. (4)).

Theorem 1. By using the left and right singular vectors of $\mathbf{K}^z = \mathbf{V}\Sigma\mathbf{U}^T$, the eigenvectors and the eigenvalues of $\widehat{\mathbf{K}}$ are computed explicitly by

$$\mathbf{\Pi} = \frac{1}{\sqrt{2}} \begin{bmatrix} \mathbf{V} & \mathbf{V} \\ \mathbf{U} & -\mathbf{U} \end{bmatrix}, \mathbf{\Lambda} = \begin{bmatrix} \Sigma & \mathbf{0}_{M \times M} \\ \mathbf{0}_{M \times M} & -\Sigma \end{bmatrix}. \quad (10)$$

Proof: Both \mathbf{V} and \mathbf{U} are orthonormal sets, therefore, $\mathbf{u}_i^T \mathbf{u}_j = \delta_{ij}$, and $\mathbf{v}_i^T \mathbf{v}_j = \delta_{ij}$, thus, the set $\{\boldsymbol{\pi}_m\}$ is orthonormal. Therefore, $\mathbf{\Pi}\mathbf{\Pi}^T = \mathbf{I}$. By using the construction defined in Eq. (10), $\mathbf{\Pi}\mathbf{\Lambda}\mathbf{\Pi}^T$ is computed explicitly by

$$\begin{aligned} \mathbf{\Pi}\mathbf{\Lambda}\mathbf{\Pi}^T &= \frac{1}{2} \begin{bmatrix} \mathbf{V} & \mathbf{V} \\ \mathbf{U} & -\mathbf{U} \end{bmatrix} \begin{bmatrix} \Sigma & \mathbf{0} \\ \mathbf{0} & -\Sigma \end{bmatrix} \begin{bmatrix} \mathbf{V}^T & \mathbf{U}^T \\ \mathbf{V}^T & -\mathbf{U}^T \end{bmatrix} = \frac{1}{2} \begin{bmatrix} \mathbf{V}\Sigma & -\mathbf{V}\Sigma \\ \mathbf{U}\Sigma & \mathbf{U}\Sigma \end{bmatrix} \begin{bmatrix} \mathbf{V}^T & \mathbf{U}^T \\ \mathbf{V}^T & -\mathbf{U}^T \end{bmatrix} = \\ & \frac{1}{2} \begin{bmatrix} \mathbf{0} & 2\mathbf{K}^z \\ (2\mathbf{K}^z)^T & \mathbf{0} \end{bmatrix} = \widehat{\mathbf{K}}. \mathbf{0} \text{ denotes the } M \times M \text{ matrix of zeros.} \end{aligned}$$

■

E. Multiview Diffusion Distance

In a variety of real data types, the Euclidian distance does not provide a sufficient indication on the intrinsic relations between data points. The Euclidian distance is highly sensitive to scaling and rotations of multidimensional data points. Tasks such as classification, clustering or system identification require a measure for the intrinsic connectivity between data points. This type of measure is only satisfied locally by the Euclidian distance in the high dimensional ambient space. The multiview diffusion kernel (defined in section (III-A)) indicates about all the small local connections between data points. The row stochastic matrix $\widehat{\mathbf{P}}^t$ (Eq. (6)) incorporates all the possibilities for having a transition in t time steps between data points that are hopping between both views. For a fixed value $t > 0$, two data points are *intrinsically similar* if the conditional distributions $\widehat{\mathbf{p}}_t(\mathbf{x}_i, \cdot) = [\widehat{\mathbf{P}}^t]_{i,\cdot}$ and $\widehat{\mathbf{p}}_t(\mathbf{x}_j, \cdot) = [\widehat{\mathbf{P}}^t]_{j,\cdot}$ are similar. This type of similarity measure indicates that the points \mathbf{x}_i and \mathbf{x}_j are similarly connected to several mutual points. Thus, they are connected by a geometrical path. In many cases, a small Euclidean distance could be misleading due to the fact that two data points could be “close” without having any Geodesic path that connects them. The similarity between probabilities is more robust in these cases.

Based on this observation, by expanding the single view construction given in [5], we define the weighted inner view diffusion distances to be

$$\mathcal{D}_t^2(\mathbf{x}_i, \mathbf{x}_j) = \sum_{k=1}^{2M} \frac{([\widehat{\mathbf{P}}^t]_{i,k} - [\widehat{\mathbf{P}}^t]_{j,k})^2}{\phi_o(k)} = \|(\mathbf{e}_i - \mathbf{e}_j)^T \widehat{\mathbf{P}}^t\|_{\widehat{\mathbf{D}}^{-1}}^2 \quad (11)$$

where \mathbf{e}_i is the i -th column of an $2M \times 2M$ identity matrix, ϕ_o is the first left eigenvector of $\widehat{\mathbf{P}}$ and its k -th element is $\phi_o(k) = \widehat{\mathbf{D}}_{k,k}$. The weighted norm of \mathbf{x} is defined by $\|\mathbf{x}\|_{\mathbf{W}} = \mathbf{x}^T \mathbf{W} \mathbf{x}$. Similarly,

$$\mathcal{D}_t^2(\mathbf{y}_i, \mathbf{y}_j) = \sum_{k=1}^{2M} \frac{([\widehat{\mathbf{P}}^t]_{M+i,k} - [\widehat{\mathbf{P}}^t]_{M+j,k})^2}{\phi_o(k)} = \|(\mathbf{e}_{M+i} - \mathbf{e}_{M+j})^T \widehat{\mathbf{P}}^t\|_{\widehat{\mathbf{D}}^{-1}}^2. \quad (12)$$

The main advantage of these distances (Eqs. (11) and (12)) is that they can be expressed in terms of the eigenfunctions and the eigenvectors of the matrix $\widehat{\mathbf{P}}$. This insight allows us to use a representation (defined in section III-F) where the induced Euclidean distance is proportional to the diffusion distances defined in Eqs. (11) and (12).

Theorem 2. The inner view diffusion distance defined by Eqs. (11) and (12) is equal to

$$\mathcal{D}_t^2(\mathbf{x}_i, \mathbf{x}_j) = 2 \cdot \sum_{\ell=1}^{M-1} \lambda_\ell^{2t} (\psi_\ell(i) - \psi_\ell(j))^2, i, j = 1, \dots, M, \quad (13)$$

and

$$\mathcal{D}_t^2(\mathbf{y}_i, \mathbf{y}_j) = 2 \cdot \sum_{\ell=1}^{M-1} \lambda_\ell^{2t} (\psi_\ell(M+i) - \psi_\ell(M+j))^2, i, j = 1, \dots, M. \quad (14)$$

Proof: We prove it for one view. The proof applies to the second view with proper adjustments. We can express $\widehat{\mathbf{P}}^t \widehat{\mathbf{D}}^{-1} (\widehat{\mathbf{P}}^t)^T$ by $\widehat{\mathbf{P}}^t \widehat{\mathbf{D}}^{-1} (\widehat{\mathbf{P}}^t)^T = \boldsymbol{\Psi} \boldsymbol{\Lambda}^t \boldsymbol{\Phi}^T \widehat{\mathbf{D}}^{-1} \boldsymbol{\Phi} \boldsymbol{\Lambda}^t \boldsymbol{\Psi}^T = \boldsymbol{\Psi} \boldsymbol{\Lambda}^{2t} \boldsymbol{\Psi}^T$ since $\boldsymbol{\Phi}^T \widehat{\mathbf{D}}^{-1} \boldsymbol{\Phi} = \mathbf{\Pi}^T \mathbf{\Pi} = \mathbf{I}$. Therefore,

$$\begin{aligned} \mathcal{D}_t^2(\mathbf{x}_i, \mathbf{x}_j) &= \|(\mathbf{e}_i - \mathbf{e}_j)^T \widehat{\mathbf{P}}^t\|_{\widehat{\mathbf{D}}^{-1}}^2 = (\mathbf{e}_i - \mathbf{e}_j)^T \widehat{\mathbf{P}}^t \widehat{\mathbf{D}}^{-1} (\widehat{\mathbf{P}}^t)^T (\mathbf{e}_i - \mathbf{e}_j) = \\ & (\mathbf{e}_i - \mathbf{e}_j)^T \boldsymbol{\Psi} \boldsymbol{\Lambda}^{2t} \boldsymbol{\Psi}^T (\mathbf{e}_i - \mathbf{e}_j) = \sum_{\ell=0}^{2M-1} \lambda_\ell^{2t} (\psi_\ell(i) - \psi_\ell(j))^2 = 2 \sum_{\ell=1}^{M-1} \lambda_\ell^{2t} (\psi_\ell(i) - \psi_\ell(j))^2. \end{aligned}$$

The final term is valid due to the repetitive form of $\widehat{\mathbf{D}}$, $\mathbf{\Pi}$, $\boldsymbol{\Psi}$ and $\boldsymbol{\Lambda}$, as described in Eq. (10). $\ell = 0$ is excluded due to $\boldsymbol{\Psi}_0 = \mathbf{1}$ (an all-ones vector) that holds for all stochastic matrices. ■

F. Multiview data parametrization

Tasks such as classification, clustering or regression in a high-dimension sampled feature space are considered to be computationally expensive. In addition, the performance of these tasks is highly dependent on the distance measure. As explained in section III-E, distance measures in the original ambient space are meaningless in many real life situations. Interpreting Theorem 2 in terms of Euclidean distance enables us to define two mappings for \mathbf{X} and \mathbf{Y} by using the right eigenvectors of $\hat{\mathbf{P}}$ (Eq. (6)) weighted by λ_i^t . A representation for \mathbf{X} is given by

$$\hat{\Psi}_t(\mathbf{x}_i) : \mathbf{x}_i \mapsto [\lambda_1^t \psi_1(i), \lambda_2^t \psi_2(i), \lambda_3^t \psi_3(i), \dots, \lambda_{M-1}^t \psi_{M-1}(i)]^T \in \mathbb{R}^{M-1} \quad (15)$$

and a representation for \mathbf{Y} is given by

$$\hat{\Psi}_t(\mathbf{y}_i) : \mathbf{y}_i \mapsto [\lambda_1^t \psi_1(M+i), \lambda_2^t \psi_2(M+i), \lambda_3^t \psi_3(M+i), \dots, \lambda_{M-1}^t \psi_{M-1}(M+i)]^T \in \mathbb{R}^{M-1}. \quad (16)$$

These mappings capture the intrinsic geometry of both views as well as the mutual relation between the views. In section III-I, we showed that the set of eigenvalues λ_m has a decaying property such that $1 = |\lambda_0| \geq |\lambda_1| \geq \dots \geq |\lambda_{M-1}|$. Exploiting the decaying property enables us to represent data up to a dimension r where $r \ll D_1, D_2$. The dimension $r \equiv r(\delta)$ is determined by approximating the diffusion distances (Eqs. (13) and (14)) up to a desired accuracy δ . This argument is expanded in section III-I.

By using the inner view diffusion distances defined in Eqs. (11) and (12), we define a convex multiview diffusion distance as a convex linear combination of the inner views distances set by parameter $0 \leq \gamma \leq 1$ such that

$$\mathcal{D}_t^{(MV)}(i, j) = \gamma \|\hat{\Psi}_t(\mathbf{x}_i) - \hat{\Psi}_t(\mathbf{x}_j)\|^2 + (1 - \gamma) \|\hat{\Psi}_t(\mathbf{y}_i) - \hat{\Psi}_t(\mathbf{y}_j)\|^2. \quad (17)$$

The parameter γ controls the influence of each view on our induced distance measure. From the application point of view, this distance is useful when one view is more reliable than the other.

G. Coupled mapping

The mappings provided by our approach (Eqs. (15) and (16)) are justified by the relations given by Eqs. (13) and (14). In this section, we provide another analytic justification for the proposed mapping. We begin with an analysis of a 1-dimensional mapping for each view. Let $\rho(\mathbf{x}) = (\rho(x_1), \rho(x_2), \dots, \rho(x_M))$ and $\rho(\mathbf{y}) = (\rho(y_1), \rho(y_2), \dots, \rho(y_M))$ denote such mappings (one for each view) and let $\hat{\rho} \triangleq (\rho(\mathbf{x}), \rho(\mathbf{y}))$ and $\hat{\rho}_i \triangleq (\rho(x_i), \rho(y_i))$. Our mapping should preserve local connectivities, therefore, we want to ensure that if the data points i and j are close in both views, then $\hat{\rho}_i$ and $\hat{\rho}_j$ will be close. Minimization of the objective function

$$\underset{\hat{\rho}}{\operatorname{argmin}} \sum_{i,j} \left[(\rho(x_i) - \rho(x_j))^2 K_{i,j}^z + (\rho(y_i) - \rho(y_j))^2 (K_{i,j}^z)^T \right] \quad (18)$$

with additional constrains provides such a connectivity preserving mapping. If $K_{i,j}^z$ is small from indicating of low connectivity between data point i and j , the distance between $\hat{\rho}_i$ and $\hat{\rho}_j$ can be large. On the other hand, if $K_{i,j}^z$ is large from indicating high connectivity between point i and j , the distance between $\hat{\rho}_i$ and $\hat{\rho}_j$ will be small to minimize the objective function.

Theorem 3. *Setting $\hat{\rho} = \psi_1$ minimizes the objective function in Eq. 18, where ψ_1 is the second eigenvector of the eigenvalue problem $\lambda_i \hat{\mathbf{P}} = \psi_i \hat{\mathbf{P}}$.*

$$\begin{aligned} \text{Proof: } & \sum_{i,j} \left[(\rho(x_i) - \rho(x_j))^2 K_{i,j}^z + (\rho(y_i) - \rho(y_j))^2 K_{i,j}^z \right] = \sum_{i,j} \rho(x_i)^2 K_{i,j}^z + \sum_{i,j} \rho(x_j)^2 (K_{i,j}^z)^T \\ & - \sum_{i,j} 2\rho(x_i)\rho(x_j)K_{i,j}^z + \sum_{i,j} \rho(y_i)^2 K_{i,j}^z + \sum_{i,j} \rho(y_j)^2 (K_{i,j}^z)^T - \sum_{i,j} 2\rho(y_i)\rho(y_j)K_{i,j}^z = \\ & \sum_i \rho(x_i)^2 D_{i,i}^{rows} + \sum_j \rho(x_j)^2 D_{j,j}^{cols} - \sum_{i,j} 2\rho(x_i)\rho(x_j)K_{i,j}^z + \\ & \sum_i \rho(y_i)^2 D_{i,i}^{cols} + \sum_j \rho(y_j)^2 D_{j,j}^{rows} - \sum_{i,j} 2\rho(y_i)\rho(y_j)K_{i,j}^z = \\ & [\rho(x) \quad \rho(y)] \left[\begin{bmatrix} \mathbf{D}^{rows} & \mathbf{0}_{M \times M} \\ \mathbf{0}_{M \times M} & \mathbf{D}^{cols} \end{bmatrix} - \begin{bmatrix} \mathbf{0}_{M \times M} & \mathbf{K}^z \\ (\mathbf{K}^z)^T & \mathbf{0}_{M \times M} \end{bmatrix} \right] \begin{bmatrix} \rho(x)^T \\ \rho(y)^T \end{bmatrix}. \end{aligned}$$

By adding a scaling constrain, the minimization problem is rewritten as

$$\underset{\hat{\rho}}{\operatorname{argmin}} \hat{\rho}(\hat{\mathbf{D}} - \hat{\mathbf{K}})\hat{\rho}^T. \quad (19)$$

$$\hat{\rho}\hat{\mathbf{D}}\hat{\rho}^T = 1$$

This minimization problem can be solved by finding the minimal eigenvalue of $(\hat{\mathbf{D}} - \hat{\mathbf{K}})\hat{\rho}^T = \bar{\lambda}\hat{\mathbf{D}}\hat{\rho}^T$ since the minimization term is $\rho\bar{\lambda}\hat{\mathbf{D}}\hat{\rho}^T = \bar{\lambda}$. This eigenproblem has a trivial solution which is an eigenvector of all ones (denoted as $\mathbf{1}$) with $\bar{\lambda} = 0$. The following constraint $\hat{\rho}\hat{\mathbf{D}}\mathbf{1} = 0$ was added to remove the trivial solution. The solution is given by the smallest non-zero

eigenvalue. Multiplying Eq. (19) by $\widehat{\mathbf{D}}^{-1}$ reduces the problem to $\widehat{\rho}\widehat{\mathbf{P}} = \lambda\widehat{\mathbf{P}}$. Thus, we are looking for the eigenvector which corresponds to the second largest eigenvalue. ■

Theorem 3 provides yet another justification to use our proposed coupled mapping.

H. Cross View Diffusion Distance

In some physical systems, the observed dataset denoted by \mathbf{X} changes over some underlying parameter denoted by α . Under this model, we can obtain multiple snapshots for various values of α . Each snapshot is denoted by \mathbf{X}_α . If these datasets are high dimensional, quantifying the amount of change in the datasets is a difficult task. This scenario was recently studied in [19]. It generalizes the diffusion framework for cases in which the data changes over the parameter α . An example of such a scenario occurs in hyper-spectral images that change over time. The DM framework is applied in [19] to a fixed value of α . Then, by using the extracted low dimensional mapping, the Euclidian distance enables to quantify the amount of changes over α . This approach is sensitive since every small change in the data can result in different mappings and the mappings are extracted independently. Thus, there is no mutual influence on the extracted mapping. Our approach incorporates the mutual relations of data within the view and the relations among views. This observation enables us to measure in a more robust way the number of variations between two datasets that correspond to a small variation in α . We now define a new diffusion distance. This distance measures the relation between two views, i.e. between all the data points. We measure the distance between all the coupled data points among both mappings by using the expression

$$\mathcal{D}_t^{(CV)^2}(X, Y) = \sum_{i=1}^M \|\widehat{\Psi}_t(\mathbf{x}_i) - \widehat{\Psi}_t(\mathbf{y}_i)\|^2. \quad (20)$$

Our kernel matrix is a product of the Gaussian kernel matrices in each view. If these values of the kernel matrices ($\mathbf{K}^x, \mathbf{K}^y$) are similar, this corresponds to similarity between the views inner geometry. The right and left singular vectors of the matrix $\mathbf{K}^x \mathbf{K}^y$ will be similar, thus, $\mathcal{D}_t^{(CV)}$ will be small.

Theorem 4. *The cross manifold distance (Eq. 20) is invariant to orthonormal transformations between the ambient spaces \mathbf{X} and \mathbf{Y} .*

Proof: Denote an orthonormal transformation matrix $\mathbf{R} : \mathbf{X} \rightarrow \mathbf{Y}$ w.l.o.g. by $\mathbf{y}_i = \mathbf{R}\mathbf{x}_i$.

$K_{i,j}^y = \exp\{-\frac{\|\mathbf{y}_i - \mathbf{y}_j\|^2}{2\sigma_y^2}\} = \exp\{-\frac{\|\mathbf{R}\mathbf{x}_i - \mathbf{R}\mathbf{x}_j\|^2}{2\sigma_y^2}\} = \exp\{-\frac{\|\mathbf{x}_i - \mathbf{x}_j\|^2}{2\sigma_x^2}\} = K_{i,j}^x$. The last equality is due to the orthonormality of \mathbf{R} and to the choice $\sigma_y = \sigma_x$. Therefore, the matrix $\mathbf{K}^z = (\mathbf{K}^x)^2$ (Eq. 4) is symmetric and its right and left singular vectors are equal, i.e. $\mathbf{U} = \mathbf{V}$, Eq.(10). This creates a repetitive form in $\Psi = \widehat{\mathbf{D}}^{-1/2} \Pi \rightarrow \psi_l(i) = \psi_l(M+i), 1 \leq i, l \leq M-1 \rightarrow \Psi_t(\mathbf{y}_i) = \Psi_t(\mathbf{x}_i)$, thus, $\mathcal{D}_t^{(CM)^2}(X, Y) = 0$. ■

I. Spectral Decay of $\widehat{\mathbf{K}}$

The power of kernel based methods for dimensionality reduction stems from the spectral decay of the kernel's eigenvalues. In this section, we study the relation between the spectral decay of the Kernel Product (Eq. (7)) and our multiview kernel (Eq. (6)). In section V-B, we evaluate the spectral decay empirically using two experiments. The rest of this section is devoted to the theoretical justification for the spectral decay of our proposed framework. We start with some background.

Theorem 5. *The eigenvalues of $\widehat{\mathbf{P}}$ (Eq. 6) are real and bounded where $|\lambda_i| \leq 1, i = 1, \dots, 2M$.*

A similar proof is given in [20].

Proof: As shown in section III-D, $\widehat{\mathbf{P}}$ is algebraically similar to a symmetric matrix, thus, its eigenvalues are guaranteed to be real. Denote by λ and ψ the eigenvalue and the eigenvector, respectively, such that $\lambda\psi = \widehat{\mathbf{P}}\psi$. Define $i_0 = \operatorname{argmax}_{1 \leq i \leq 2M} |\psi(i)|$ to be the index of the largest entry in ψ . The maximal value $\psi(i_0)$ can be computed using $\widehat{\mathbf{P}}$ from Eq. 6 such that $\lambda\psi(i_0) = \sum_{j=1}^{2M} \widehat{P}_{i_0 j} \psi(j) \rightarrow |\lambda| = |\sum_{j=1}^{2M} \widehat{P}_{i_0 j} \frac{\psi(j)}{\psi(i_0)}| \leq \sum_{j=1}^{2M} \widehat{P}_{i_0 j} \frac{|\psi(j)|}{|\psi(i_0)|} \leq \sum_{j=1}^{2M} \widehat{P}_{i_0 j} = 1$. The first inequality is due to the triangle inequality and the second equality is due to the kernel normalization by $\widehat{\mathbf{D}}^{-1}$. ■

Theorem 5 shows that the eigenvalues are bounded. However, bounded eigenvalues are insufficient for dimensionality reduction. Dimensionality reduction is meaningful when there is a significant spectral decay.

Definition 1. *Let \mathcal{M} be a manifold. The intrinsic dimension d of the manifold is a positive integer determined by how many independent "coordinates" are needed to describe \mathcal{M} . Using a parametrization to describe a manifold, the dimension of \mathcal{M}*

is the smallest integer d such that a smooth map $f(\xi) = \mathcal{M}$, $\xi \in \mathcal{R}^d$, describes the manifold, where $\xi \in \mathcal{R}^d$.

Our framework is based on a Gaussian kernel. The spectral decay of Gaussian kernels was studied in [5]. We use Lemma 2 to evaluate the spectral decay of our kernel.

Lema 2. Assume that the data is sampled from a manifold with intrinsic dimension $d \ll M$. Let \mathbf{K}° (section III-B) denotes the kernel with an exponential decay as a function of the Euclidean distance. For $\delta > 0$, the number of eigenvalues of \mathbf{K}° above δ is proportional to $(\log(\frac{1}{\delta}))^d$.

Lemma 2 is based on Weyl's asymptotic law [21]. Let $r_\delta = r(\delta) = \max\{\ell \in N \text{ such that } |\lambda_\ell| \geq \delta\}$ denotes the number of eigenvalues of \mathbf{K}° above δ . $K_{i,j}^\circ = K_{i,j}^x K_{i,j}^y$ corresponds to a single DM view given in [5]. Theorem 6 relates the spectral decay of the kernel \widehat{P} (Eq. 6) to the decay of the Kernel Product-based DM (P° Eq. (7) and in [5]).

Lema 3. Let $\mathbf{X}, \mathbf{Y} \in \mathbb{R}^{M \times M}$ be such that $\mathbf{X}, \mathbf{Y} \geq 0$. Then for any $1 \leq k \leq M - 1$

$$\prod_{\ell=k}^{M-1} \lambda_\ell(\mathbf{X}\mathbf{Y}) \leq \prod_{\ell=k}^{M-1} \lambda_\ell(\mathbf{X} \circ \mathbf{Y}) \quad (21)$$

where \circ is the Kronecker matrix product.

This inequality is proved in [22] and [23].

Theorem 6. Multiplying the last $M - 1 - r_\delta$ eigenvalues of \mathbf{K}^z is smaller than δ^{M-1-r_δ} . Formally, $\prod_{\ell=r_\delta}^{M-1} \lambda_\ell(\mathbf{X}\mathbf{Y}) \leq \delta^{M-1-r_\delta}$.

Proof: Denote by $\{\lambda_i(\mathbf{X})\}_{i=0}^{M-1}$ the eigenvalues of the matrix \mathbf{X} . They are enumerated in descending order such that $\lambda_0(\mathbf{X}) \geq \lambda_2(\mathbf{X}) \geq \dots \geq \lambda_{M-1}(\mathbf{X})$. We use Lemma 3 to prove Theorem 6 by choosing $\mathbf{X} = \mathbf{K}^x$ and $\mathbf{Y} = \mathbf{K}^y$, which are positive semi-definite. $\mathbf{K}^x \circ \mathbf{K}^y = \mathbf{K}^\circ$ corresponds to the approach in [5]. By using Lemma 3 and choosing $\ell = r_\delta$ in Eq. 21, we get

$$\prod_{\ell=r_\delta}^{M-1} \lambda_\ell(\mathbf{K}^x \mathbf{K}^y) \leq \prod_{\ell=r_\delta}^{M-1} \lambda_\ell(\mathbf{K}^\circ) \leq \delta^{M-1-r_\delta}.$$

Using the kernel matrix spectral decay, we can approximate Eqs. (13) and (14) by neglecting all the eigenvalues that are smaller than δ . Thus, we can compute a low dimensional mapping such that

$$\widehat{\Psi}_t^r(\mathbf{x}_i) : \mathbf{x}_i \longmapsto [\lambda_1^t \psi_1(i), \lambda_2^t \psi_2(i), \lambda_3^t \psi_3(i), \dots, \lambda_{r-1}^t \psi_{r-1}(i)]^T \in \mathbb{R}^{r-1}. \quad (22)$$

This mapping of dimension r provides a low dimensional space which improves the performance and the efficiency of various machine learning tasks.

J. More than two views

In this paper, we focus on coupled views scenario, however this approach can be applied to more views. In this section, we present the algebraic steps required to handle more than two views. Denote the l -th view by \mathbf{X}^l , $l = 1, \dots, L$. Each view is a high dimensional dataset $\mathbf{X}^l = \{\mathbf{x}_1^l, \mathbf{x}_2^l, \mathbf{x}_3^l, \dots, \mathbf{x}_M^l\} \in \mathbb{R}^{M \times N}$. As presented in Section III-A, the first step is to choose symmetrical positive semi-definite kernels for each view $\mathcal{K}^l : \mathbf{X}^l \times \mathbf{X}^l \longrightarrow R$, $l = 1, \dots, L$, then the generalized multiview kernel is formed by the following matrix

$$\widehat{\mathbf{K}} = \begin{bmatrix} \mathbf{0}_{M \times M} & \mathbf{K}^1 \mathbf{K}^2 & \mathbf{K}^1 \mathbf{K}^3 & \dots & \mathbf{K}^1 \mathbf{K}^p \\ \mathbf{K}^2 \mathbf{K}^1 & \mathbf{0}_{M \times M} & \mathbf{K}^2 \mathbf{K}^3 & \dots & \mathbf{K}^2 \mathbf{K}^p \\ \mathbf{K}^3 \mathbf{K}^1 & \mathbf{K}^3 \mathbf{K}^2 & \mathbf{0}_{M \times M} & \dots & \mathbf{K}^3 \mathbf{K}^p \\ \vdots & \vdots & \vdots & \dots & \vdots \\ \mathbf{K}^p \mathbf{K}^1 & \mathbf{K}^p \mathbf{K}^2 & \mathbf{K}^p \mathbf{K}^3 & \dots & \mathbf{K}^p \mathbf{K}^p \end{bmatrix}, \quad (23)$$

Then, by using the diagonal matrix $\widehat{\mathbf{D}}$ where $\widehat{D}_{i,i} = \sum_j \widehat{K}_{i,j}$, the normalized row-stochastic matrix becomes

$$\widehat{\mathbf{P}} = \widehat{\mathbf{D}}^{-1} \widehat{\mathbf{K}}, \quad \widehat{P}_{i,j} = \frac{\widehat{K}_{i,j}}{\widehat{D}_{i,i}}, \quad (24)$$

where the m, l block (square $M \times M$ matrix located at $[1 + (m - 1)M, 1 + (l - 1)M]$, $l = 1, \dots, L$) describes the probability of transition between view \mathbf{X}^m and \mathbf{X}^l . As explained in section III-D, the eigenvalues of the matrix $\widehat{\mathbf{P}}$ could be computed using the SVD of the block matrices. Therefore, $p - 1$ decompositions are needed for each of the appropriate $M \times M$ block.

IV. INFINITESIMAL GENERATOR

A family of diffusion operators were introduced in [5]. Each operator differs by the normalization. If appropriate limits are taken such that $M \rightarrow \infty$, $\epsilon \rightarrow 0$ and $\epsilon = 2\sigma^2$, then from [5], the DM kernel operator will converge to one of the following differential operators: 1. Normalized graph Laplacian. 2. Laplace Beltrami diffusion. 3. Heat kernel equation. These are proved in [5]. These are all special cases of the diffusion equation. This provides not only a physical justification for the DM framework, but allows in some cases to distinguish between the geometry and the density of the data points. In this section, we study the asymptotics properties of the proposed kernel $\widehat{\mathbf{K}}$ (Eq. 5).

Theorem 7. *The infinitesimal generator induced by the proposed kernel $\widehat{\mathbf{K}}$ (Eq. 5) converges when $M \rightarrow \infty$, $\epsilon \rightarrow 0$, $\epsilon = 2\sigma^2$ to a “cross domain Laplacian operator”. The convergence is to functions $f(x)$ and $g(y)$, which are the eigenfunction of $\widehat{\mathbf{K}}$. These functions operate on the two manifolds \mathcal{M}_x and \mathcal{M}_y and are the solutions to the following diffusion like equations:*

$$\begin{aligned} g(y) &= [m_1 f(y) + m_2 f''(y)], \\ f(x) &= [m_3 g(x) + m_4 g''(x)]. \end{aligned}$$

Proof: Assume x_1, x_2, \dots, x_M are i.i.d uniformly distributed on some manifold \mathcal{M}_x and y_1, y_2, \dots, y_M are i.i.d uniformly distributed on another manifold \mathcal{M}_y . The functions $f(x)$ and $g(y)$ are used to construct the vector

$$\mathbf{h} = [f(x_1), f(x_2), \dots, f(x_M), g(y_1), g(y_2), \dots, g(y_M))] \in \mathbb{R}^{2M}$$

. The limit of the characteristic equation is

$$\lim_{\substack{M \rightarrow \infty \\ \epsilon = 2\sigma_x^2 = 2\sigma_y^2 \rightarrow 0}} g(y_i) - \frac{\sum_{j=1}^M K_{ij}^z f(x_j)}{\sum_{j=1}^M K_{ij}^z} = \lim_{\substack{M \rightarrow \infty \\ \epsilon \rightarrow 0}} g(y_i) - \frac{\sum_{j=1}^M \sum_{l=1}^M e^{-\frac{\|x_i - x_j\|^2}{2\sigma_x^2}} e^{-\frac{\|y_l - y_j\|^2}{2\sigma_y^2}} f(x_j)}{\sum_{j=1}^M K_{ij}^z}.$$

The sum is approximated by using the following Riemann-based integral

$$\frac{1}{M} \sum_{j=1}^M \sum_{l=1}^M e^{-\frac{\|x_i - x_j\|^2}{2\sigma_x^2}} e^{-\frac{\|y_l - y_j\|^2}{2\sigma_y^2}} f(x_j) \xrightarrow{M \rightarrow \infty} \int \int e^{-\frac{(y-t)^2}{2\sigma_y^2}} e^{-\frac{(x-t)^2}{2\sigma_x^2}} f(x) dx dt.$$

By applying a change of variables $z = \frac{x-t}{\sigma_x}$, $x = z\sigma_x + t$, $dx = dz\sigma_x$, we get

$$\int \int e^{-\frac{(y-t)^2}{2\sigma_y^2}} e^{-\frac{(x-t)^2}{2\sigma_x^2}} f(x) dx dt = \sigma_x \int \int e^{-\frac{z^2}{2\sigma_x^2}} e^{-\frac{(t-y)^2}{2\sigma_y^2}} f(t + z\sigma_x) dz dy.$$

By using Taylor's expansion of f we get

$$\begin{aligned} &= \sigma_x \int \int e^{-\frac{z^2}{2\sigma_x^2}} e^{-\frac{(t-y)^2}{2\sigma_y^2}} [f(t) + f'(t)z\sigma_x + \frac{1}{2}f''(t)z^2\sigma_x^2 + \dots] dz dy \\ &\approx \sigma_x \int e^{-\frac{(t-y)^2}{2\sigma_y^2}} [\int e^{-\frac{z^2}{2}} f(t) + \int e^{-\frac{z^2}{2}} f'(t)z\sigma_x + \frac{1}{2} \int e^{-\frac{z^2}{2}} f''(t)z^2\sigma_x^2] dz dy \\ &= \sigma_x \int e^{-\frac{(t-y)^2}{2\sigma_y^2}} [a_0 f(t) + \frac{1}{2} a_1 f''(t) \sigma_x^2] dz dy, \end{aligned}$$

where $a_0 = \int e^{-\frac{z^2}{2}} dz = \sqrt{2\pi}$, $\int e^{-\frac{z^2}{2}} z dz = 0$ and $a_1 = \int e^{-\frac{z^2}{2}} z^2 dz = \sqrt{2\pi}$.

By another change of variables, $r = \frac{t-y}{\sigma_y}$, $t = r\sigma_y + y$, $dt = dr\sigma_y$, we get

$$\begin{aligned} &= \sigma_x \int e^{-\frac{r^2}{2}} [a_0 f(y + r\sigma_y) + \frac{1}{2} a_1 f''(y + r\sigma_y) \sigma_x^2] dr \\ &\approx \sigma_x \int e^{-\frac{r^2}{2}} [a_0 [f(y) + f'(y)r\sigma_y + \frac{1}{2} f''(y)r^2\sigma_y^2] + \frac{1}{2} a_1 \sigma_x^2 [f''(y) + f'''(y)r\sigma_y + \frac{1}{2} f''''(y)r^2\sigma_y^2]] dr \\ &\approx \sigma_x [a_0 \int e^{-\frac{r^2}{2}} f(y) dr + \frac{1}{2} \int e^{-\frac{r^2}{2}} f''(y) (r^2\sigma_y^2 + a_1\sigma_x^2) dr] \\ &= \sigma_x [a_0^2 f(y) + a_3 f''(y)], \end{aligned}$$

where $a_3 = \int e^{-\frac{r^2}{2}} (r^2\sigma_y^2 + a_1\sigma_x^2) dr = \sqrt{2\pi}(\sigma_y^2 + \sigma_x^2)$. We neglected the order σ^4 terms. In the same way, we compute the eigenfunctions $g(x)$

$$f(x) = \sigma_y [a_0^2 g(x) + a_4 g''(x)].$$

This infinitesimal generator is a coupled Laplacian operator acting on the manifolds. The characteristic functions induced by this operator are sines and cosines, just as in the standard diffusion equation. ■

V. EXPERIMENTAL RESULTS

In this section, we present the experimental results that evaluate our framework. The first experiment demonstrates the advantage of our method for spectral clustering. The second experiment evaluates the spectral decay rate of our proposed method. The third experiment evaluates the cross domain diffusion distance. The fourth experiment demonstrates how the proposed approach extracts coupled embeddings from coupled views. The final experiment demonstrates the proposed approach on a real data set.

A. Experiment I: Spectral Clustering

Spectral properties of data sets are useful for clustering since they reveal information about the unknown number of clusters. The characteristic of the eigenvalues of \hat{P} (Eq. 6) can provide insight into the number of clusters within the data set. The study in [24] relates the number of clusters to the multiplicity of the eigenvalue 1. A different approach in [25] provides an analysis about the relation between the eigenvalue drop to the number of clusters. In this section, we evaluate how our proposed method captures the clusters' structure when two views are available.

We generate two circles that represent the original clusters using the function

$$\mathbf{Z} = \begin{bmatrix} z_i^1 \\ z_i^2 \end{bmatrix} = \begin{bmatrix} r \cos(\theta_i) \\ r \sin(\theta_i) \end{bmatrix}, \quad (25)$$

where 1600 points $\theta_i, 1 \leq i \leq 1600$, are spread linearly within the line $[0, 4\pi]$. The clusters are created by changing the radius as follows: $r = 2.2, 1 \leq i \leq 800$ (first cluster), $r = 4, 801 \leq i \leq 1600$ (second cluster). The views \mathbf{X} and \mathbf{Y} are generated by the application of the following non-linear functions to generate the distorted views

$$x_i^1 = \begin{cases} z_i^1 + 0.8 + n_i^2 |z_i^2| \geq 0 \\ z_i^1 - 0.8 + n_i^3 |z_i^2| < 0 \end{cases}, x_i^2 = z_i^2 + n_i^1 \quad (26)$$

and

$$y_i^1 = z_i^1 + n_i^4, y_i^2 = \begin{cases} z_i^2 + 0.8 + n_i^5 |z_i^1| \geq 0 \\ z_i^2 - 0.8 + n_i^6 |z_i^1| < 0 \end{cases}, \quad (27)$$

where $n_i^l, 1 \leq l \leq 6$, are i.i.d random variables drawn from a Gaussian distribution with $\mu = 0$ and $\sigma_n = 0.35$. This data is referred as the Coupled Circles dataset.

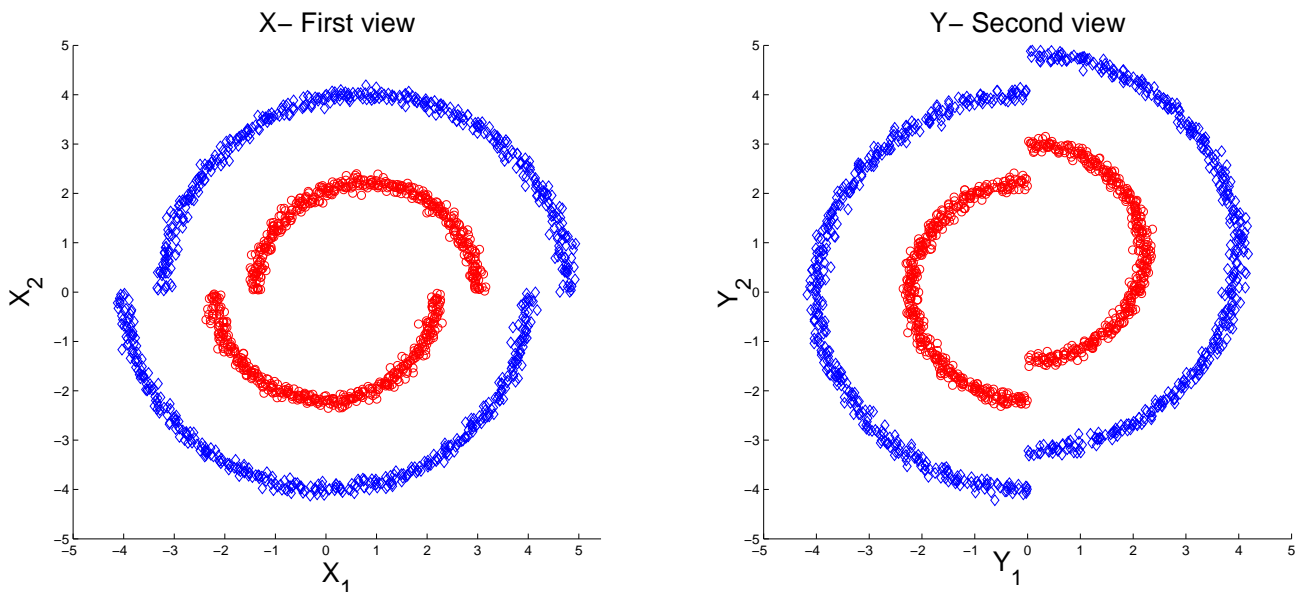


Fig. 2: Left: first view \mathbf{X} . Right: second view \mathbf{Y} . The ground truth clusters are represented by the marker's shape and color.

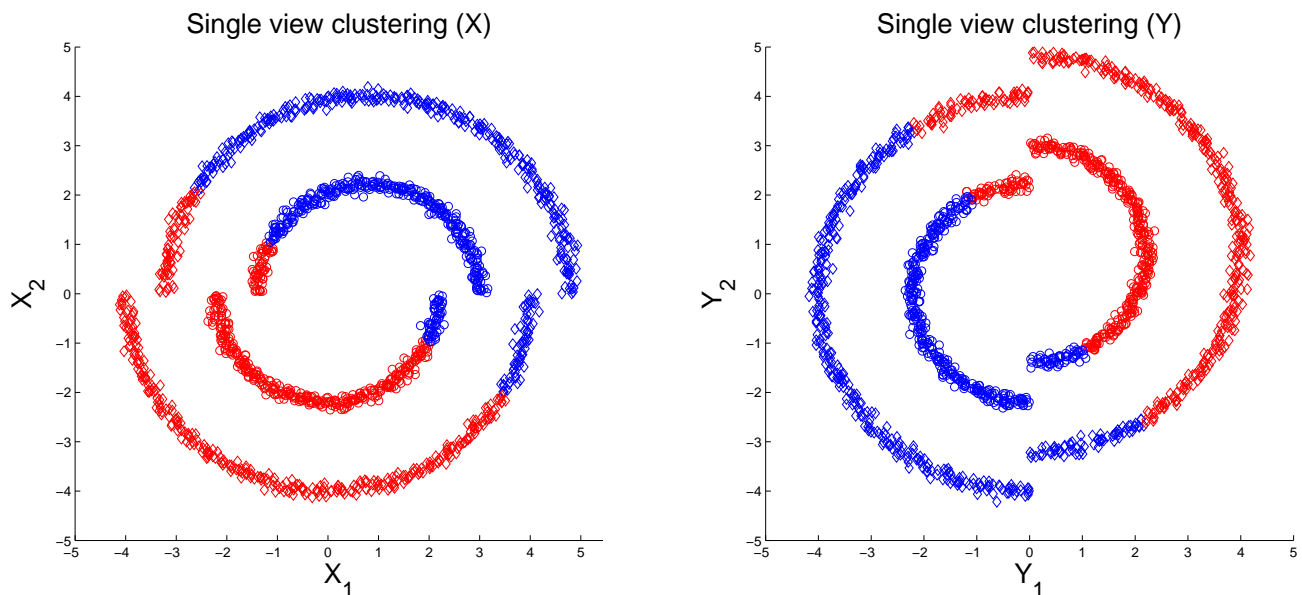


Fig. 3: Left: first view X . Right: second view Y . The ground truth clusters are represented by the marker's shape. The clustering results, which are based on the single DM-based view, are represented by the marker's color.

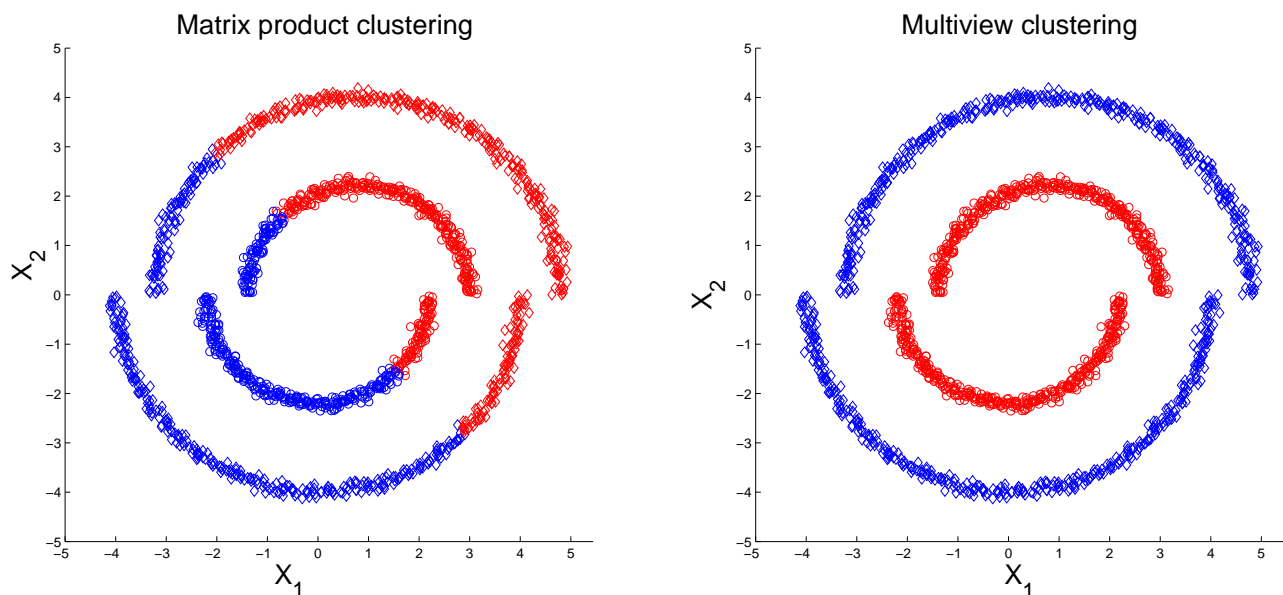


Fig. 4: Left: first view X . The clustering result, which originated from a DM-based Kernel Product, are represented by the marker's color. Right: first view X . The clustering results, which are based on the proposed approach, are represented by the marker's color. The ground truth clusters are represented by the marker's shape.

In Fig. 2, the views X and Y , which were generated by Eqs. (26) and (27), are presented. Color and shape indicate the ground truth classes. Initially, DM is applied to each view and it performs clustering by using K-means ($k = 1$) within the first diffusion coordinate. The following parameters $t = 1, \sigma_x = \sigma_y = 0.05$ are used. They are defined in the DM framework Section II-B. The results are presented in Fig. 3. We further extract a 1-dimensional representation using the proposed multiview framework (Eq. 15) and the DM-based Kernel Product (Eq. 7). Clustering is performed in the representation space by the application of K-means where $k = 1$. In the multiview mapping, the following parameters $t = 1, \sigma_x = \sigma_y = 0.05$ (defined in Eq. 4 and 15) and $\sigma^\circ = 0.071$ (Eq. 8) are used. The clustering results are presented in Fig. 4. It is evident that the multiview-based approach outperforms the DM-based single view and the Kernel Product approaches. To evaluate the performance of our proposed mapping, 100 simulations with various values of the Gaussian's noise variance (all with zero mean) were performed. The average clustering success rate is presented in Fig. 5.

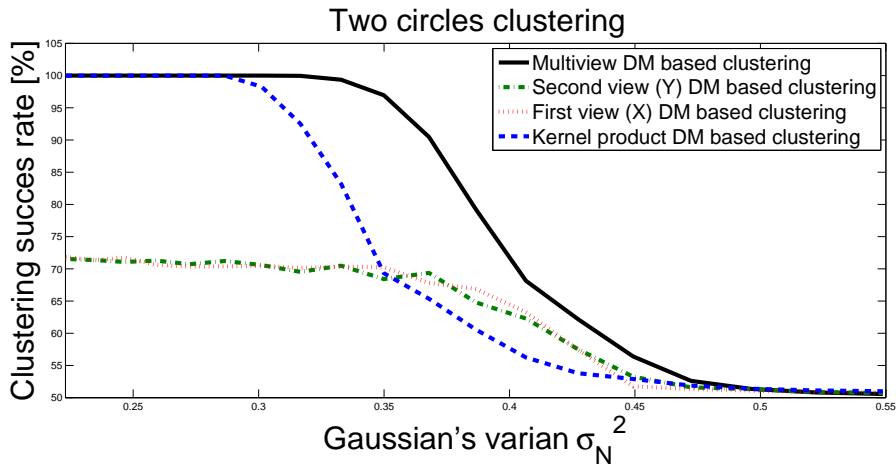


Fig. 5: Clustering results from averaging 100 trials vs. the variance of the Gaussian noise. The simulation performed on the Coupled Circles data (Eqs. (25), (26) and (27)).

B. Experiment II: Spectral Decay

In Section III-I, an upper bound on the eigenvalues' decay rate for our multiview-based approach (matrix \hat{P} Eq. (6)) is presented. In order to empirically evaluate the decay rate, synthetic datasets are generated accompanied by comparison to other approaches. To evaluate the spectral decay of \hat{P} (Eq. (6)), P° (Eqs. (7) and [5]) and P^+ (Eq. (9)) we compare the spectral decay rate between various frameworks on synthetic clustered data drawn from Gaussian distributions. The following steps describe the generation of both views denoted by (\mathbf{X}, \mathbf{Y}) and referred as View-I (\mathbf{X}) and View-II (\mathbf{Y}), respectively:

- 1) 6 vectors $\mu_j \in \mathbb{R}^9$, $j = 1, \dots, 6$ were drawn from a Gaussian distribution $N(\mathbf{0}, 8 \cdot \mathbf{I}_{9 \times 9})$. These vectors are the center of masses of the generated classes.
- 2) 100 data points were drawn for each cluster j by using μ_j , $1 \leq j \leq 6$, from another Gaussian distribution $N(\mu_j, 2 \cdot \mathbf{I}_{9 \times 9})$. Denote these 600 data points by \mathbf{X} .
- 3) 100 data points were drawn for each cluster j by using μ_j , $1 \leq j \leq 6$, from another Gaussian distribution $N(\mu_j, 2 \cdot \mathbf{I}_{9 \times 9})$. Denote these 600 data points by \mathbf{Y} .

The first 3 dimensions of both views are presented in Fig. 6. We compute the probability matrix for each view P^x and P^y (Eq. (1)), the Kernel Sum approach probability matrix P^+ (Eq. (9)), the Kernel Product approach P° (Eq. (7)) and the proposed approach \hat{P} . The eigendecomposition is computed for all matrices. The resulting eigenvalues' decay rate are compared with the eigenvalues product from both views. To get a fair comparison between all the methods, we set the Gaussian scale parameter σ_x and σ_y in each view and then use these scales in all the methods. The vectors' variance in the concatenation approach is the sum of variances since we assume statistical independence. Therefore, the following scale parameters $\sigma_\circ^2 = \sigma_x^2 + \sigma_y^2$ are used.

The experiment is repeated but this time \mathbf{X} contains 6 clusters whereas \mathbf{Y} contains only 3. For \mathbf{Y} , we use only the first center of masses and generate 200 points in each cluster. Figure 7 presents a logarithmic scale of the spectral decay for eigenvalues extracted from all methods. It is evident that our proposed kernel has the strongest spectral decay.

C. Experiment III: Cross View Diffusion Distance

In this section, we examine the proposed Cross View Diffusion Distance (Section III-H). A swiss roll is generated by using the function

$$\text{View I: } \mathbf{X} = \begin{bmatrix} x_i^1 \\ x_i^2 \\ x_i^3 \end{bmatrix} = \begin{bmatrix} 6\theta_i \cos(\theta_i) \\ h_i \\ 6\theta_i \sin(\theta_i) \end{bmatrix} + \mathbf{N}_i^1, \quad (28)$$

$\theta_i = (1.5\pi)s_i$, $i = 1, 2, 3, \dots, 1000$, where s_i are 1000 data points that spread linearly within the line $s_i \rightarrow [1, 3]$. The second view is generated by the application of an orthonormal transformation to the swiss roll and by adding Gaussian noise. The function in Eq. (29) describes the representation of the second view:

$$\text{View II: } \mathbf{Y} = \begin{bmatrix} y_i^1 \\ y_i^2 \\ y_i^3 \end{bmatrix} = \mathbf{R} \begin{bmatrix} 6\theta_i \cos(\theta_i) \\ h_i \\ 6\theta_i \sin(\theta_i) \end{bmatrix} + \mathbf{N}_i^2 \quad (29)$$

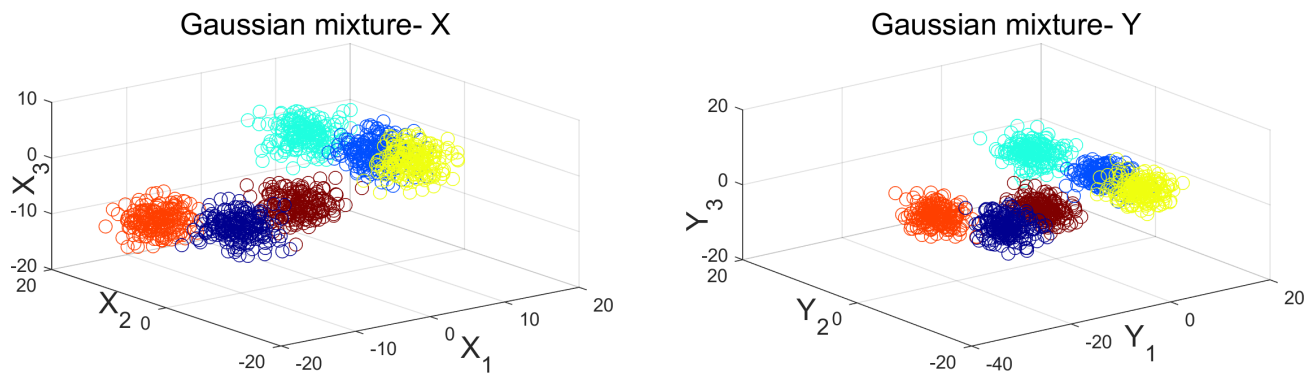


Fig. 6: The first 3 dimensions of the Gaussian mixture. Both views share the center of masses of the Gaussian spread. Left: first view denoted as \mathbf{X} . Right: second view denoted as \mathbf{Y} . The variance of the Gaussian in each dimension is 8.

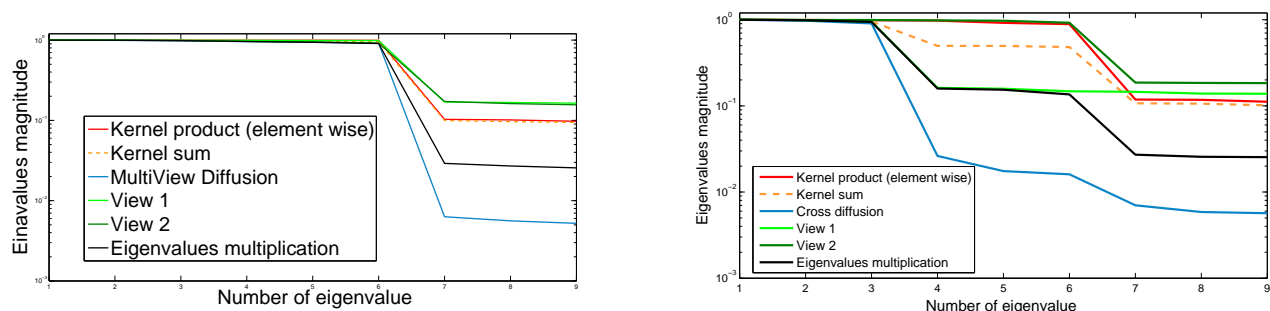


Fig. 7: Eigenvalues decay rate. Comparison between different mapping methods. Left: 6 clusters in each view. Right: 6 clusters in \mathbf{X} and 3 clusters in \mathbf{Y} .

where $\mathbf{R} \in \mathbb{R}^{3 \times 3}$ is a random orthonormal transformation matrix. It is generated by drawing values from i.i.d Gaussian variables and by the application of Graham-Schmidt. $h_i, i = 1, \dots, 1000$ are drawn from a uniform distribution within the interval $[0, 100]$. Each component of $\mathbf{N}_i^1, \mathbf{N}_i^2 \in \mathbb{R}^{3 \times 1}$ is drawn from a Gaussian distribution with zero mean and a variance of σ_N . An example for both Swiss rolls is presented in Fig. 8. The standard DM is applied to each view and a 2-dimensional

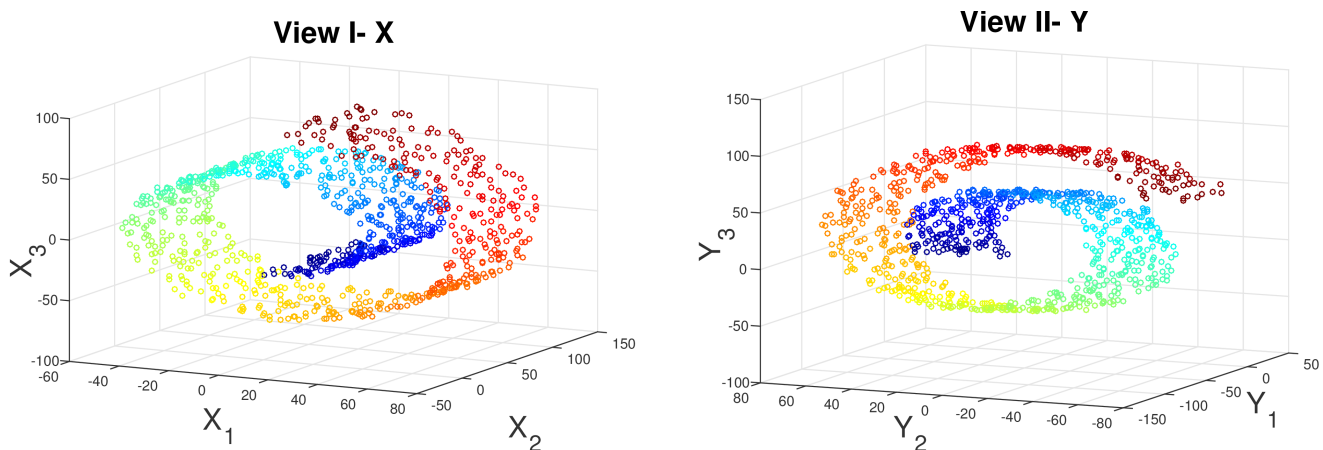


Fig. 8: The two Swiss Rolls, Top- generated by Eq. (28), Bottom- generated by Eq. (29).

embedding of the Swiss roll is extracted. The sum of distances between all the data points in the embedding spaces is denoted as a single view diffusion distance (SVDD). The distance is computed using Eq. 30:

$$\mathcal{D}_t^{(SV)}(X, Y) = \sum_{i=1}^M \|\Psi_t(\mathbf{x}_i) - \Psi_t(\mathbf{y}_i)\|^2. \quad (30)$$

The proposed framework is applied to extract the coupled embedding. The Cross View Diffusion Distance (CVDD) is computed using Eq. (20). This experiment was executed 100 times for various values of the Gaussian noise variance. The median of the results are presented in Fig. 9. In about 10% of the single view simulations the embeddings' axis are permuted. This generates a large SVDD although the embeddings share similar structures. In order to remove these measurements we present the Median of 100 simulations.

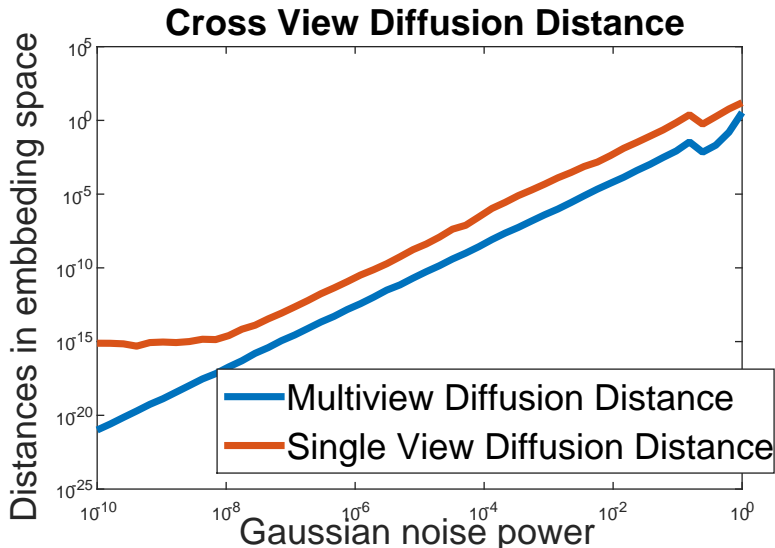


Fig. 9: Comparison between two cross view diffusion based distances. Simulated on two Swiss rolls with additive Gaussian noise. The results are the median of 100 simulations.

D. Experiment IV: Coupled Manifold Learning

In the general DM approach, there is an assumption that the sampled space describes a low dimensional manifold. However, this assumption can be incorrect since the sampled space can describe the existence of redundancy in the manifold, or more generally, the sampled space can describe two or more manifolds generated by a common physical process. In this section, we examine the extracted embedding computed using our method and compare it to the Kernel Product approach (section III-B).

Helix A

Two coupled manifolds with a common underlying open circular structure are generated. The helix shaped manifolds were generated by the application of a 3 dimensional function to 1000 data points that spread linearly within the lines $a_i \rightarrow [0, 2\pi]$ and $b_i = a_i + 0.5\pi \bmod 2\pi$, $i = 1, 2, 3, \dots, 1000$. The functions in Eqs. (31) and (32) are used to generate the datasets for View-I and View-II denoted as \mathbf{X} and \mathbf{Y} , respectively:

$$\text{View I: } \mathbf{X} = \begin{bmatrix} x_i^1 \\ x_i^2 \\ x_i^3 \end{bmatrix} = \begin{bmatrix} 4 \cos(0.9a_i) + 0.3 \cos(20a_i) \\ 4 \sin(0.9a_i) + 0.3 \sin(20a_i) \\ 0.1(6.3a_i^2 - a_i^3) \end{bmatrix}, i = 1, 2, 3, \dots, 1000, \quad (31)$$

$$\text{View II: } \mathbf{Y} = \begin{bmatrix} y_i^1 \\ y_i^2 \\ y_i^3 \end{bmatrix} = \begin{bmatrix} 4 \cos(0.9b_i) + 0.3 \cos(20b_i) \\ 4 \sin(0.9b_i) + 0.3 \sin(20b_i) \\ 0.1(6.3b_i - b_i^2) \end{bmatrix}, i = 1, 2, 3, \dots, 1000. \quad (32)$$

The 3-dimensional Helix shaped manifolds \mathbf{X} and \mathbf{Y} are presented in Fig. 10.

The Kernel Product mapping (Eq. (7)) separates the manifold to a bow and a point as shown in Fig. 12. This structure neither represents any of the original structures nor reveals the underlying parameters a_i, b_i . On the other hand, our embedding (Eqs. (15) and (16)) captures the two structures one for each view. As shown in Fig. 11, one structure represents the angle of a_i while the other represents the angle of b_i . The Euclidean distance in the new spaces preserves the mutual relations between data points based on the geometrical relation in both views. Moreover, both manifolds are in the same coordinate system and this is a strong advantage as it enables us to compare between the manifolds in the lower dimensional space. The Euclidean distance in the new spaces preserves the mutual relations between data points that are based on the geometrical structure of both views.

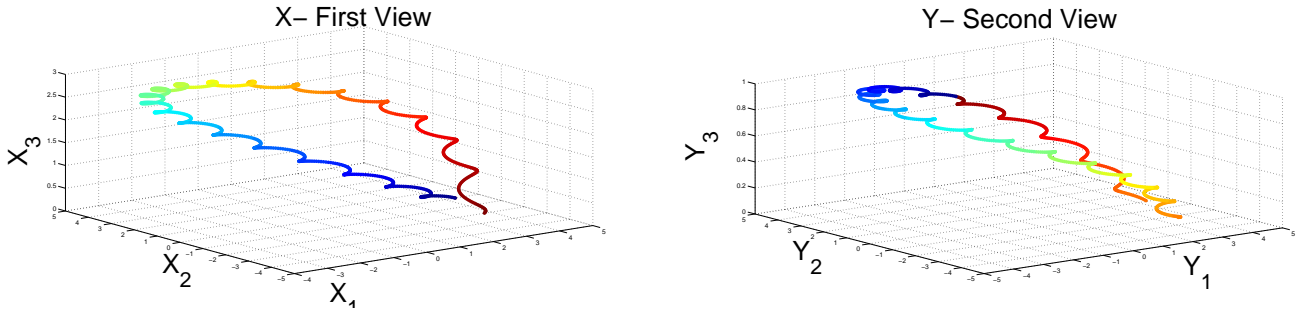


Fig. 10: Left: first Helix \mathbf{X} (Eq. (31)). Right: second Helix \mathbf{Y} (Eq. (32)). Both manifolds have some circular structure governed by the angle parameter a_i and b_i , $i = 1, 2, 3, \dots, 1000$ colored by the points index i .

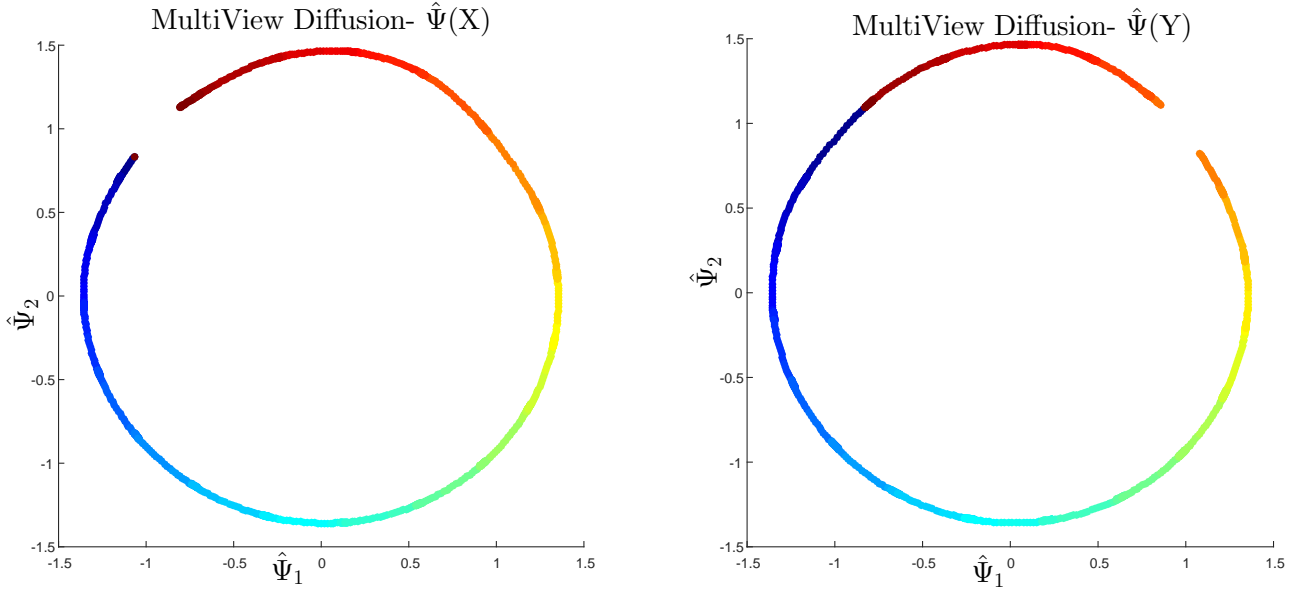


Fig. 11: Left: MultiView based embedding of the first view $\hat{\Psi}(\mathbf{X})$. Right: MultiView based embedding of the second view $\hat{\Psi}(\mathbf{Y})$. They were computed by using Eqs. (15) and (16), respectively.

Helix B

The previous experiment was repeated with the functions in Eqs. (33) and (34) to generate datasets for View-I and View-II denoted by \mathbf{X} and \mathbf{Y} , respectively.

$$\text{View I: } \mathbf{X} = \begin{bmatrix} x_i^1 \\ x_i^2 \\ x_i^3 \end{bmatrix} = \begin{bmatrix} 4 \cos(5a_i) \\ 4 \sin(5a_i) \\ 4a_i \end{bmatrix}, \quad (33)$$

$$\text{View II: } \mathbf{Y} = \begin{bmatrix} y_i^1 \\ y_i^2 \\ y_i^3 \end{bmatrix} = \begin{bmatrix} 4 \cos(5b_i) \\ 4 \sin(5b_i) \\ 4b_i \end{bmatrix}. \quad (34)$$

Again, 1000 points were generated using $a_i \rightarrow [0, 2\pi]$, $b_i = a_i + 0.5\pi \pmod{2\pi}$, $i = 1, 2, 3, \dots, 1000$. The generated manifolds are presented in Fig. 13.

As can be viewed in Fig. 14, the proposed embeddings (Eqs. (15) and (16)) has successfully captured the governing parameters a_i and b_i . The Kernel Product based embedding (Eq. (7)) is presented in Fig. 15. The Kernel Product based embedding again separated the data points into two unconnected structures that do not represent well the parameters.

E. MultiView Video Sequence

Various examples such as images, audio, MRI [18], [7] and [26] have demonstrated the power of DM for extracting from real datasets the underlying changing physical parameters. In this experiment, the multiview approach is tested on a real data.

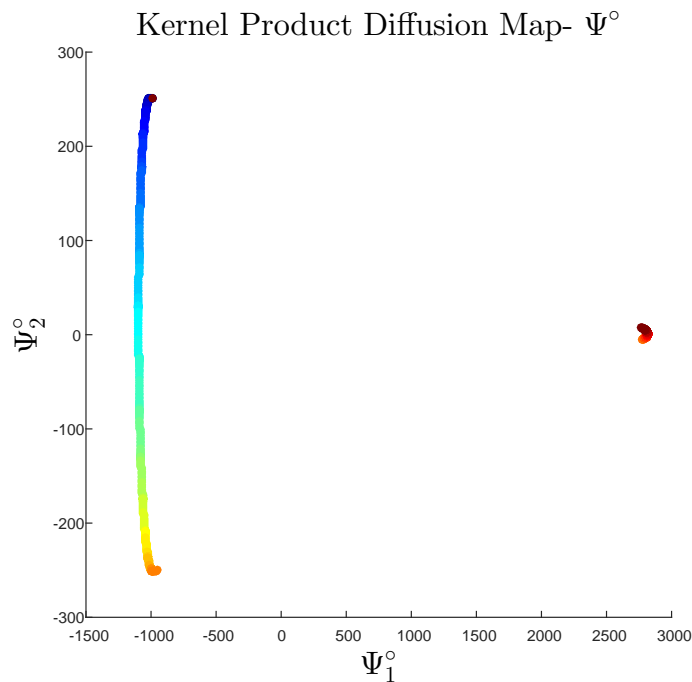


Fig. 12: 2-dimensional DM-based mapping of the Helix computed using the concatenation vector from both views that correspond to the kernel P° (Eq.(7)).

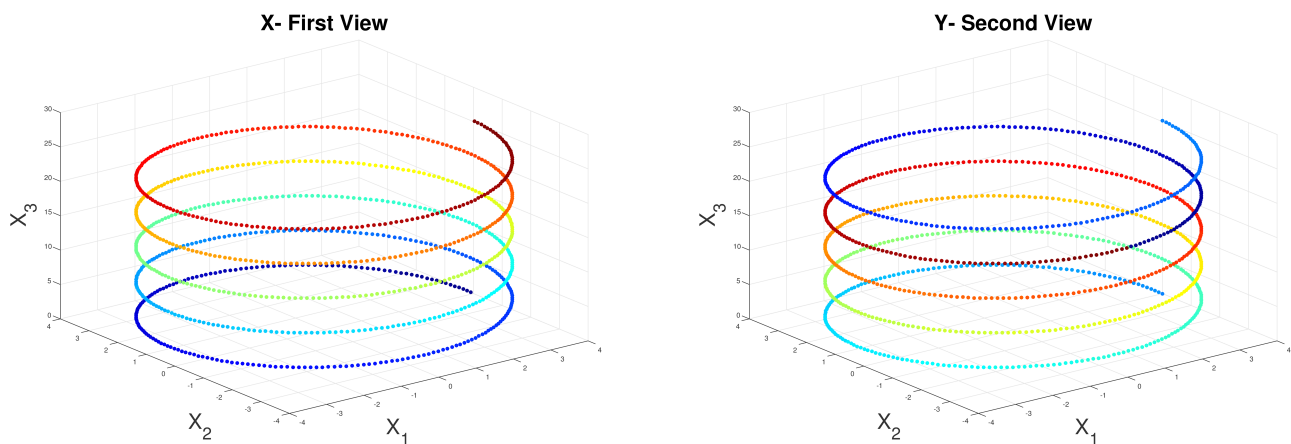


Fig. 13: Left: first Helix \mathbf{X} (Eq. (33)). Right: second Helix \mathbf{Y} (Eq. (34)). Both manifolds have some circular structure governed by the angle parameter a_i and b_i , $i = 1, 2, 3, \dots, 1000$, as colored by the point's index i .

Two web cameras and a toy train with a pre-designed path are used. The train's path has an "eight" shape structure. Extracting the underlying manifold from the set of images enables us to organize the images according to the location along the train's path and thus reveals the true underlying parameters of the processes.

The setting of the experiment is as follows: each camera records a set of images from a different angle. A sample frame from each view is presented in Fig. 16. The video is sampled at 30 frames per second with a resolution of 640×480 pixels per frame. $M = 220$ images were collected from each view (camera). Then, the R,G,B values were averaged and downsampled to 160×120 pixels resolution. The matrices were reshaped into column vectors. The resulted set of vectors are denoted by \mathbf{X} and \mathbf{Y} where $x_i, y_i \in R^{19200}$, $1 \leq i \leq 220$. The sequential order of the images is not important for the algorithm. In a normal setting, one view is sufficient to extract the parameters that govern the movement of the train and thus extract the natural order of the images. However, we use two types of interferences to create a scenario in which each view by itself is insufficient for the extraction of the underlying parameters. The first interference is a gap in the recording of each camera. We remove 20 consecutive frames from each view at different time locations. By doing it, the bijective correspondence of some of the images in the sequence is broken. However, even an approximated correspondence is sufficient for our proposed manifold extraction.

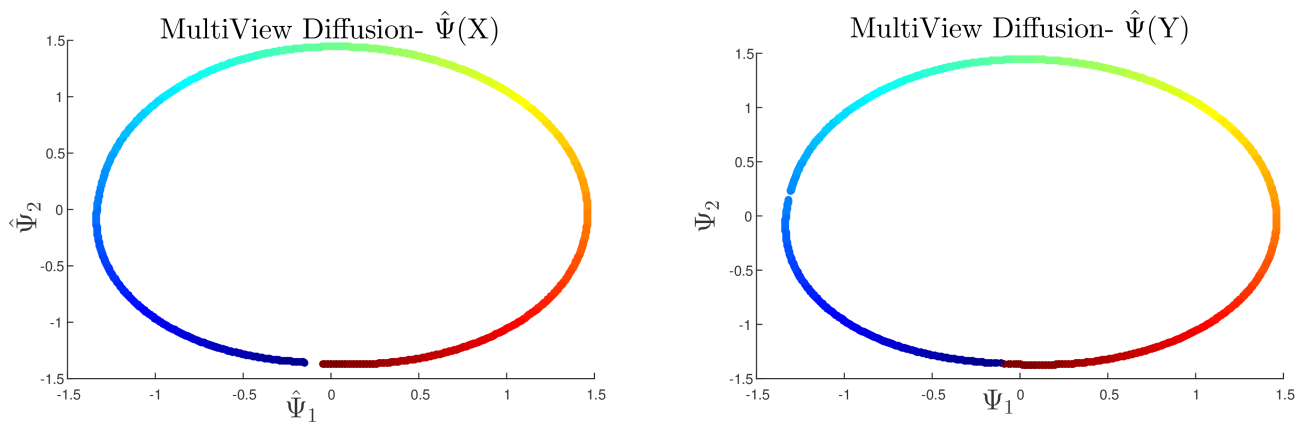


Fig. 14: The coupled mappings computed using our proposed parametrization in Eqs. 15 and 16.

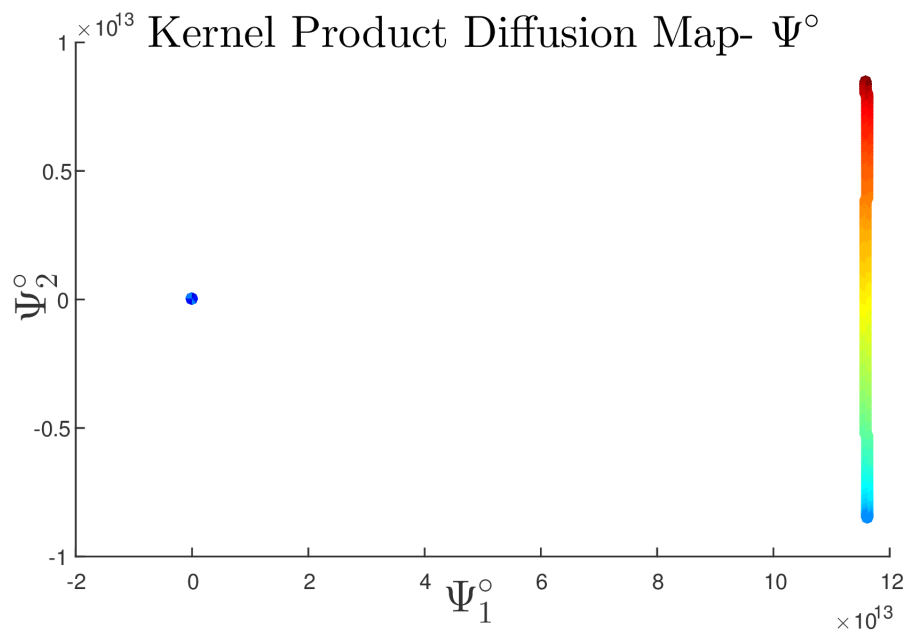


Fig. 15: A 2-dimensional mapping, extracted based on P° (Eq. (7)).

A standard 2-dimensional DM base mapping of each view was extracted. The results are bow shaped manifolds as presented in Fig. 17. Applying DM separately to each view extracts the correct order of the data points (images) along the path. However, the “missing” data points broke the circular structure of the expected manifold and resulted in a bow shaped embedding. We use the multiview-based methodology to overcome this interference by application of the multiview-based framework to extract two coupled mapping (Eqs. (15) and (16)). The results are presented in Fig. 18. The proposed approach overcomes the interferences by smoothing the gap inherited in each view through the use of connectivities from the “undistracted” view. Finally, we concatenate the vectors from both views and compute the Kernel Product embedding. The results are presented in Fig. 19. Again, the structure of the manifold is distorted and incomplete due to the missing images.

This experiment was repeated while replacing 10 frames from each view with a Gaussian noise that has the parameters $\mu = 0$ and $\sigma^2 = 10$ that are average and variance, respectively. A single view DM-based mapping was computed. The Kernel Product-based DM and the multiview-based DM mappings were computed as well. As presented in Fig. 20, the Gaussian noise distorted the manifolds extracted in each view. The multiview approach extracted two circular structures presented in Fig. 21. Again, the data points are ordered according to the position along the path. This time, the circular structure is unfolded and the gaps are visible in both embeddings. The application of the Kernel Product approach (Eq. 7) yielded again a distorted manifold as presented in Fig. 22.



Fig. 16: Left: a sample image from the first camera (X). Right: a sample image from the second camera (Y).

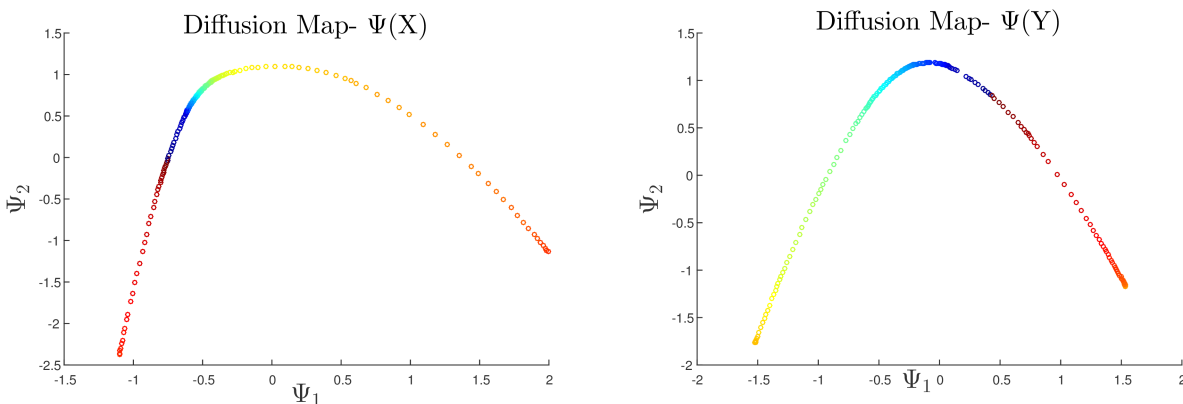


Fig. 17: Left: DM-based single view mapping $\Psi(X)$. Right: DM-based single view mapping $\Psi(Y)$). The removed images caused a bow shaped structure.

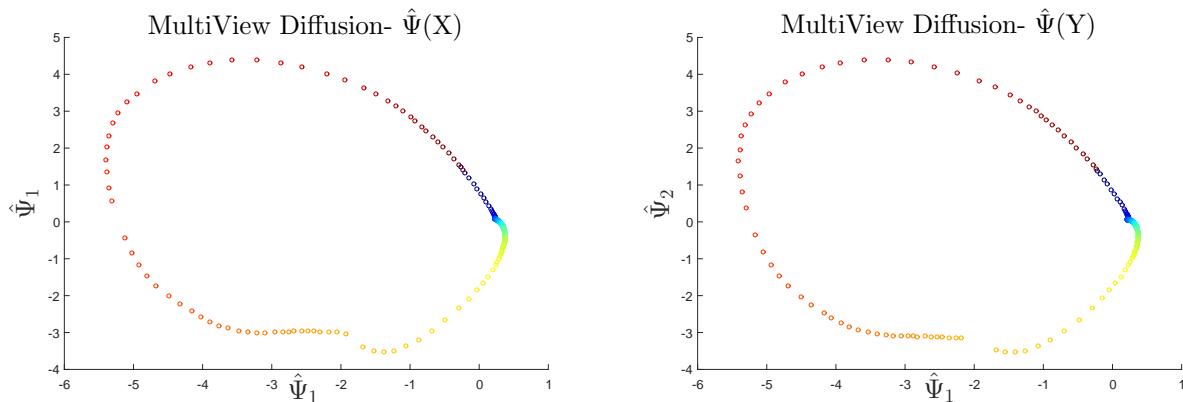


Fig. 18: Left: Mapping $\hat{\Psi}(X)$. Right: Mapping $\hat{\Psi}(Y)$ as extracted by the multiview-based framework. Two small gaps, which correspond to the removed images, are visible

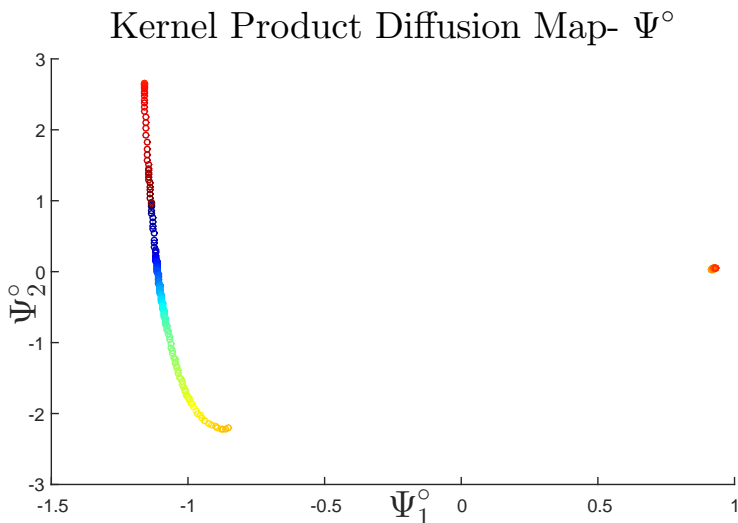


Fig. 19: A standard diffusion mapping (Kernel Product-based) that was computed by using the concatenation vector from both views that correspond to kernel K° .

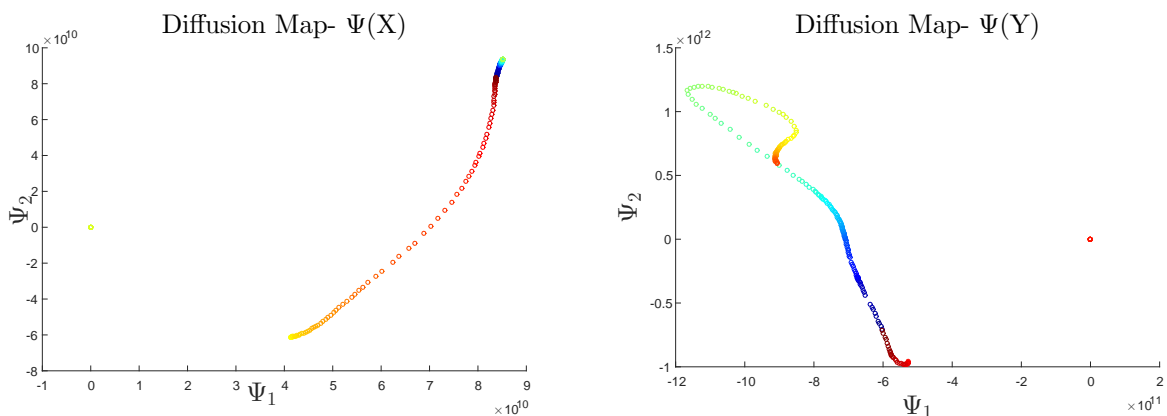


Fig. 20: Left: DM-based single view mapping $\Psi(X)$. Right: DM-based single view mapping $\Psi(Y)$. The Gaussian noise deformed the circular structure

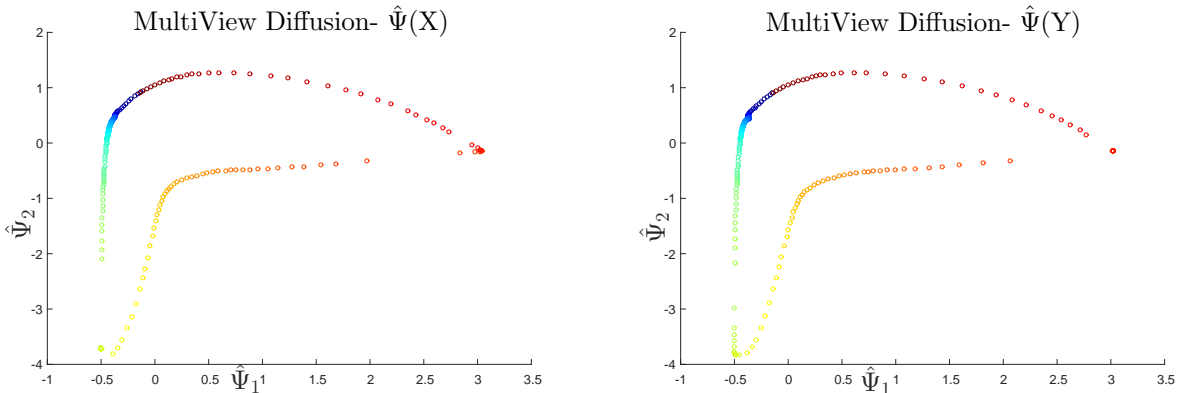


Fig. 21: Left: Mapping $\hat{\Psi}(X)$. Right: Mapping $\hat{\Psi}(Y)$ as extracted by the multiview framework. Two gaps are visible that correspond to Gaussian noise.

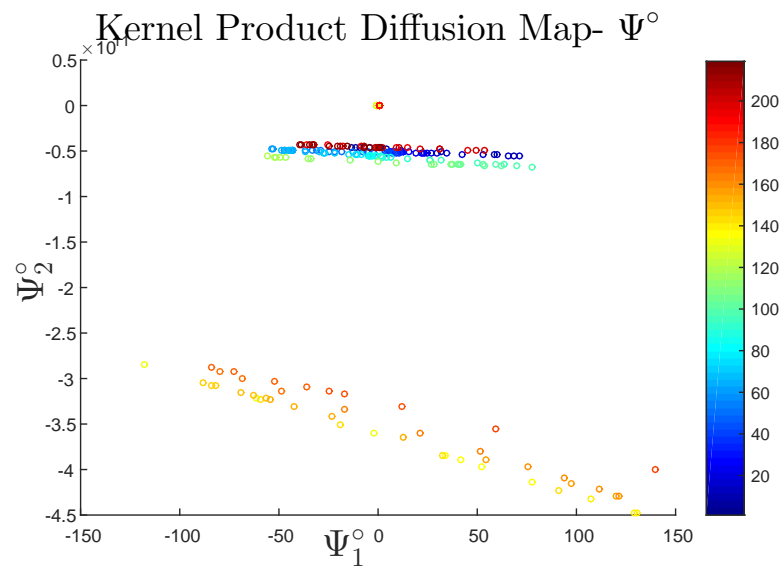


Fig. 22: Computation of a standard diffusion mapping (Kernel Product) by using the concatenation vector from both views (corresponding to kernel P° Eq.(7)).

VI. CONCLUSIONS

In this paper, we presented a framework for dimensionality reduction that is multiview based. The method enables us to extract simultaneous embeddings from coupled embeddings. We enforce a cross domain probabilistic model at a single time step. The transition probabilities depend on the connectivities in both views. We derived various theoretical aspects of the proposed method and demonstrated their applicabilities to both artificial and real data. The experimental results demonstrate the strength of the proposed framework in cases where data is missing in each view or each of the manifolds is deformed by an unknown function. The framework is applicable to various real life machine learning tasks that consist of multiple views or multiple modalities. We consider the influence of various normalizations methods on the extracted embedding. Future work will include both application and theoretical analysis of such normalizations.

REFERENCES

- [1] I. Jolliffe, *Principal component analysis*, 2005, vol. 21.
- [2] J. B. Kruskal and W. M., "Multidimensional scaling," *Sage Publications. Beverly Hills*, 1977.
- [3] S. T. Roweis and L. K. Saul, "Nonlinear dimensionality reduction by local linear embedding," *Science*, vol. 290.5500, pp. 2323–2326, 2000.
- [4] W. Luo, "Face recognition based on laplacian eigenmaps," 2011, pp. 416 – 419.
- [5] R. R. Coifman and S. Lafon, "Diffusion maps," *Applied and Computational Harmonic Analysis*, vol. 21, pp. 5–30, 2006.
- [6] A. Singer and R. R. Coifman, "Non linear independent component analysis with diffusion maps," *Applied and Computational Harmonic Analysis*, vol. 25(2), pp. 226–239, 2008.
- [7] O. Lindenbaum, A. Yeredor, and I. Cohen, "Musical key extraction using diffusion maps," *Signal Processing*, 2015.
- [8] W. T. Freeman and J. B. Tenenbaum, "Learning bilinear models for two-factor problems in vision," in *Computer Vision and Pattern Recognition, Proceedings., IEEE Computer Society Conference on. IEEE*, 1997, pp. 554–560.
- [9] I. S. Helland, "Partial least squares regression and statistical models," *Scandinavian Journal of Statistics*, pp. 97–114, 1990.
- [10] K. Chaudhuri, S. M. Kakade, K. Livescu, and K. Sridharan, "Multi-view clustering via canonical correlation analysis," in *Proceedings of the 26th annual international conference on machine learning. ACM*, 2009, pp. 129–136.
- [11] A. Kumar, P. Rai, and H. Daume, "Co-regularized multi-view spectral clustering," in *Advances in Neural Information Processing Systems*, 2011, pp. 1413–1421.
- [12] D. Zhou and C. Burges, "Spectral clustering and transductive learning with multiple views," *Proceedings of the 24th international conference on Machine learning*, pp. 1159–1166, 2007.
- [13] B. Wang, J. Jiang, W. Wang, Z.-H. Zhou, and Z. Tu, "Unsupervised metric fusion by cross diffusion," in *Computer Vision and Pattern Recognition (CVPR), 2012 IEEE Conference on. IEEE*, 2012, pp. 2997–3004.
- [14] A. Kumar and H. Daumé, "A co-training approach for multi-view spectral clustering," in *Proceedings of the 28th International Conference on Machine Learning (ICML-11)*, 2011, pp. 393–400.
- [15] B. Boots and G. Gordon, "Two-manifold problems with applications to nonlinear system identification," 2012.
- [16] H. Hotelling, "Relations between two sets of variates," *Biometrika*, pp. 321–377, 1936.
- [17] V. R. de Sa, "Spectral clustering with two views," in *ICML workshop on learning with multiple views*, 2005.
- [18] S. Lafon, Y. Keller, and R. Coifman, "Data fusion and multicue data matching by diffusion maps," *IEEE Trans. Pattern Anal. Mach. Intell.*, vol. 28 no. 11, p. 17841797, 2006.
- [19] M. Hirn and R. Coifman, "Diffusion maps for changing data," *Applied and computational harmonic analysis*, 2013.
- [20] S. Yoel. Lector notes on spectral methods in data anlysis, <https://sites.google.com/site/yoelshkolnisky/teaching>.
- [21] S. Lafon, "Diffusion maps and geometric harmonics," *Ph.D dissertation Yale*, 2004.
- [22] T. Ando, "Majorization relations for hadamard products." *Linear Algebra and its Applications*, pp. 57–64, 1995.
- [23] G. Visick, "A weak majorization involving the matrices a , b and ab ." *Linear Algebra and its Applications*, vol. 224/224, pp. 731–744, 1995.
- [24] A. Y. Ng, M. I. Jordan, and Y. Weiss, "On spectral clustering1 analysis and an algorithm," *Proceedings of Advances in Neural Information Processing Systems. Cambridge, MA: MIT Press*, vol. 14, pp. 849–856, 2001.
- [25] M. Polito and P. Perona, "Grouping and dimensionality reduction by locally linear embedding," in *NIPS*, 2001, pp. 1255–1262.
- [26] G. Piella, "Diffusion maps for multimodal registration," *Sensors*, vol. 14, no. 6, pp. 10562–10577, 2014.